WIDE BANDGAP DEVICE BASED MULTIPHASE MOTOR DRIVE WITH HIGH

ACCELERATION CAPABILITY

A Dissertation

by

AJAY KUMAR MORYA

Submitted to the Office of Graduate and Professional Studies of
Texas A&M University
in partial fulfillment of the requirements for the degree of

DOCTOR OF PHILOSOPHY

Chair of Committee,	Hamid Toliyat
Committee Members,	Prasad Enjeti
	Shankar P. Bhattacharyya
	Won-Jong Kim
Head of Department,	Miroslav M. Begovic

December 2018

Major Subject: Electrical Engineering

ABSTRACT

Electric vehicles require high transient torque to start and accelerate faster. Moreover, many industrial drives like those used with weaving machines, conveyors, cargo handling, hoists, and printing presses also require high transient torque. This dissertation presents the invention of a system reconfiguration and control technique for a multiphase motor drive to obtain up to 93% higher torque for acceleration. Wide bandgap (WBG) devices enable the next-generation efficient and lightweight motor drives for use in industrial, automotive, ship propulsion, aerospace, and rail applications. This dissertation provides a comprehensive review of the different major ac motor drive applications that would benefit from WBG devices. This dissertation also discusses the technical challenges, converter design considerations and design trade-offs in realizing the full potential of WBG devices in motor drives. There is a trade-off between high switching frequency and other issues such as high dv/dt and electromagnetic interference. The problem of high common mode currents, bearing damage and insulation damage caused by high dv/dt are discussed. Silicon Carbide (SiC) and Gallium Nitride (GaN) inverters are designed, built and tested for motor drive applications and the performance is validated with experimental results.

To achieve transient peak torque higher rated current needs to be forced into the motor for short duration. The duration of overload is determined by the magnitude of current during overload and the thermal characteristics of the motor. The switching devices of power electronics converter cannot be overloaded. Therefore, transient peak

torque capability of an electric drive is limited by the power electronics converter. The invention presented in this dissertation makes it possible to achieve 93% higher transient torque in a multiphase motor drive. The superior acceleration capability of the invention is validated with experimental results. SiC and GaN inverters are used to drive an induction motor. Both the inverters are able to operate at switching frequency of 200 kHz.

To my parents

ACKNOWLEDGEMENTS

CONTRIBUTORS AND FUNDING SOURCES

NOMENCLATURE

BEV   Battery Electric Vehicle

CM   Common Mode

CMTI   Common Mode Transient Immunity

DSP   Digital Signal Processor

EMC   Electromagnetic Compatibility

EMF   Electromotive Force

EMI   Electromagnetic Interference

ESL   Equivalent Series Inductance

ESR   Equivalent Series Resistance

EV   Electric Vehicle

FEM   Finite Element Method

FOM   Figure of Merit

GaN   Gallium Nitride

HEMT   High Electron Mobility Transistor

IC   Integrated Circuit

IFOC   Indirect Field Oriented Control

IGBT   Insulated Gate Bipolar Transistors

IM   Induction Motor

IMD   Integrated Motor Drive

IPMSM   Interior Permanent Magnet Synchronous Motor

MIM	Multiphase Induction Motor
MOSFET	Metal Oxide Semiconductor Field Effect Transistors
MTBF	Mean Time Between Failure
MTL	Multi-conductor Transmission Line Model
MTPA	Maximum Torque Per Ampere
NASA	National Aeronautics and Space Administration
PCB	Printed Circuit Board
PHEV	Plug-in Hybrid Electric Vehicle
PI	Proportional Integral
PPM	Pole Phase Modulation
PWM	Pulse Width Modulation
RLC	Resistor-Inductor-Capacitor
RMS	Root Mean Square
Si	Silicon
SiC	Silicon Carbide
SPDT	Single Position Double Throw
STR	Subtransient Time Rating
VSD	Variable Speed Drive
VSI	Voltage Source Inverters
WBG	Wide Bandgap

TABLE OF CONTENTS

x

LIST OF FIGURES

xiii

LIST OF TABLES

1. INTRODUCTION

Significant research efforts have been focused on development of wide bandgap (WBG) semiconductor devices [1]-[3] and their applications in power electronics [4], [5]. The primary advantages of WBG devices result from their low losses, high switching frequency and high-temperature operation capability [3], [4]. Many countries aim to reduce air pollution and lower their dependence on fossil fuel vehicles. China, India, France, Great Britain and Norway have already announced plans to ban cars with internal combustion engines in the coming decades and replace them with vehicles powered by clean energy. Therefore, the demand for both battery electric vehicles (BEVs) and plug-in hybrid electric vehicles (PHEVs) is expected to increase 10-fold between 2017 and 2027 [6]. Wide bandgap (WBG) devices are a key technology for vehicle electrification. Therefore, WBG semiconductors have great prospects and their market is expected to top $10 billion, with majority of the demand coming from the BEV and PHEV sector [6].

Silicon Carbide (SiC) and Gallium Nitride (GaN) are the two most prominent WBG materials for power devices. Table 1.1 shows some important properties of SiC and GaN devices [1], [7]. The higher critical electric field ($\geq$ 200 V/μm) in WBG materials enables thinner and highly doped voltage-blocking layers in the devices, which can reduce on-resistance by two orders of magnitude relative to Silicon (Si), which has a critical electric field of 30 V/μm, in majority carrier devices like metal oxide semiconductor field effect transistors (MOSFETs) [3]. The low intrinsic carrier concentration of WBG materials, which is less than 10^{-9}/cm^3, results in low leakage currents, even at high

temperatures, which enables robust high-temperature performance [3]. The figure of merit (FOM) is defined as the product of the on-state resistance and gate charge for a switch, so a lower FOM corresponds to better performance [8]. WBG devices have much lower FOMs than Si devices. For example, a GaN transistor has three to seven times better FOM than a Si MOSFET [8]

Table 1.1. Properties of wide bandgap devices.

Property	Si	GaN	SiC
Bandgap (eV)	1.1	3.4	3.2
Electron mobility (cm^2/Vs)	1450	2000	900
Critical electric field (MV/cm)	0.3	3.5	3.0
Electron saturation velocity (10^7 cm/s)	1.0	2.5	2.2
Thermal conductivity (W/cm-K)	1.5	1.3	5.0
Maximum operating temperature (°C)	200	300	600
Specific heat capacity (J/KgK)	712	490	681

WBG devices are enabling high power, low-inductance motors that require a high switching frequency and a high-bandwidth current regulation strategy to obtain an acceptable current ripple, which is typically lower than 5% for many applications [9]. Along with the recent technological advances in motors, SiC devices are enabling the next generation of high-speed, direct-drive medium-voltage drives for megawatt (MW) class motors in many critical energy applications [10], [11]. The primary applications are in petroleum refining industries, natural gas infrastructure, and other industrial applications [12]. The demand for high-speed motors for drilling, milling, grinding, and machining

applications, turbo compressors, and flywheels is increasing. WBG-based converters have lower losses at the high switching frequencies required for these motors when compared to Si-based converters. This makes the system more efficient, lightweight, and compact, which is particularly important in portable applications. Another class of electric drives benefitting from WBG devices is motor drives operating in high-temperature environments. Hybrid electric vehicles (HEVs), sub-sea and down-hole pump applications, deep earth drilling, combat electric vehicles, space crafts, and national aeronautics and space administration (NASA) probes and landers for space exploration are typical examples of drives in high-temperature environment [13]-[15]. To extract maximum performance from WBG devices and minimize electromagnetic interference, specific hardware design considerations need to be followed.

Electric drives used in electric and hybrid electric vehicles, electric locomotive traction, electric ship propulsion, more-electric aircraft and industrial electric drives used in weaving machines, conveyors, cargo handling, hoists, printing presses require short-term high torque [16], [17]. The variable speed drives (VSDs) for these applications are designed to provide short-time overload capability to meet transient torque requirements. The time taken to go from 0-60 miles per hour (mph) speed is an important specification for an electric car and all car manufacturers are competing to make this time smaller [18].

To achieve transient peak torque higher rated current needs to be forced into the motor for short duration. The duration of overload is determined by the magnitude of current during overload and the thermal characteristics of the motor [19]. The switching devices of power electronics converter cannot be overloaded. Therefore, transient peak

torque capability of an electric drive is limited by the power electronics converter, which needs to be designed with devices rated for higher current.

Multiphase machines have reduced toque ripple, higher power density than three-phase motors [20]. Using WBG devices, the inverter can be integrated with the multiphase motor thus avoiding use of multiple ac cables, so only two dc link cables will be required. Low losses and the high junction temperature of WBG devices make it possible to integrate the inverter and the motor.

For a typical hybrid electric vehicle (HEV) and electric vehicle (EV) driving cycle, the drivetrain is lightly loaded most of the time [21]. Therefore, the vehicle-level fuel efficiency is significantly reduced by lower light load efficiency of Si insulated gate bipolar transistors (IGBTs). SiC MOSFETs, which have high efficiency even at light loads, can greatly improve the fuel economy of HEVs and EVs [21].

1.1   Wide Bandgap Devices for Motor Drives

The WBG devices can provide significant benefits for many applications, especially low-inductance motors, high-speed motors, and electric drives operating in high-temperature environment. Low-inductance motors generally require a pulse width modulation (PWM) frequency of 50-100 kHz or higher to keep the current ripple within acceptable limits [22]. Current ripple is undesirable because it wastes energy in the motor windings and may cause unwanted pulsations in the torque. For low-inductance motors rated at a few kilowatts, Si MOSFETs can be used because they can provide the desired current ripple by switching at up to 50 kHz [23]. At power levels higher than a few kilowatts, Si IGBTs are preferred over MOSFETs, but the switching frequency of a Si

IGBT is limited to about 20 kHz [24], [25], which fails to meet the current ripple limitations in low-inductance motors. Thus, due to their high switching frequency capability, WBG devices enable low-inductance motors rated for high power [26].

High-speed electric machines are gaining popularity in industry due to their high power density [27]. The worldwide push for electrification of transportation systems is also fueling the advance of high-speed machine technologies. The fundamental frequency required by high-speed machines can be several kilohertz (kHz). The high switching frequency capability of WBG devices enables high-speed machines with a larger number of poles, which can reduce the weight and volume. MW-level (>1000 HP), high-speed (10,000-20,000 rpm) motors are used in petroleum refining industries, natural gas infrastructure, and other industrial applications. Deployment of medium-voltage variable speed drives in these MW class motors could provide significant energy savings of up to 0.7% to 1.8% of the total US electricity consumption [28].

The maximum operating temperature of a semiconductor material is determined by its bandgap. Therefore, semiconductors with a wider bandgap can operate at higher temperatures. However, to this point, the current unavailability of high temperature packaging has limited the present SiC modules to 200 °C [29]. Additionally, SiC has a higher thermal conductivity than Si, allowing SiC devices to dissipate heat produced by losses faster, so SiC devices can operate at much higher power densities than Si devices. With the increased demand for high efficiency, high power density, and high-temperature capabilities in aerospace and automotive applications, integrated motor drives (IMDs) offer a promising solution [30]. IMDs also offer direct replacement for inefficient direct
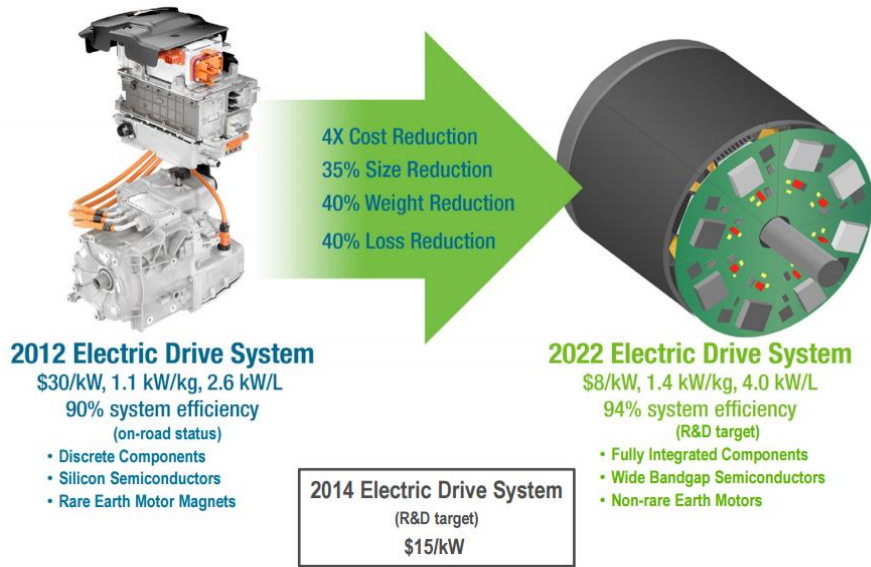
Figure 1.1. US DOE 2022 electric drive system target for an electric vehicle, reprinted from [31].

on-line motors. Close physical integration of the converter and the machine results in a temperature increase in the power electronic components, which limits power levels to 7.5 kW with Si-based IMDs [30]. WBG devices with their high-temperature capability make IMDs feasible for higher power levels. Figure 1.1 shows the 2022 electric drive system target set by the United States department of energy (DOE) in its advanced power electronics and electric motor research and development program [31]. The high efficiency and power density targets are achievable with WBG device-based IMD approach. In 2018, Tesla unveiled an electric drivetrain using 650 V, 100 A SiC MOSFETs for its Model 3 car. Figure 1.2 shows the main inverter of Tesla Model 3 car, which uses 24 SiC MOSFET modules from ST Microelectronics; 4 devices connected in parallel for each switch position [32]. The modules are molded modules using copper ribbon bonding for MOSFET connections.

6
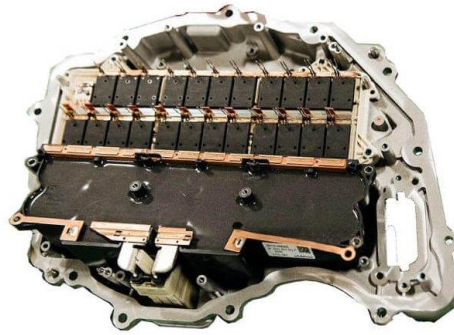
Figure 1.2. Tesla Model 3 3-phase inverter driving propulsion motor, reprinted from [32].

To justify the higher cost of WBG devices and fully realize their potential, they must be switched at high speeds, but high switching speeds result in additional electromagnetic interference (EMI) generation. High *dv/dt* excites the capacitive coupling paths in converter, cables and motor causing substantial common mode (CM) current to flow and can damage motor insulation.

1.2 Control of Multiphase Motor Drives

An n-phase machine can be represented using n/2 orthogonal subspaces for machines with an even number of phases and (n − 1)/2 orthogonal subspaces for machines with an odd number of phases using the vector space decomposition approach. The orthogonal subspace includes one α–β subspace and several x–y subspaces, and the zero-sequence components [33]. For a machine with sinusoidal magnetomotive force distribution, only the α–β components contribute to torque production, while x–y and zero-sequence components only produce losses. Generally, zero-sequence components can be neglected, since the neutral point of the machine is generally isolated so that the zero-sequence currents cannot flow. Controlling only the torque and flux producing α–β

currents is insufficient and additional controllers are necessary to minimize the x–y currents that can flow due to the inverter dead-time effect [34] and asymmetry in converter or motor. Among the multiphase machines, machines having multiple three phase windings (6, 9 and 12 phases) are most popular. The modular three-phase structures allows the use of the well-established three-phase technology. In this dissertation, we are using an asymmetrical six-phase machine, which has $30°$ spatial shift between the two three-phase stator windings with isolated neutral points. The x–y currents that have physical meaning in asymmetrical six-phase machine can be interpreted as the circulating currents between the two three phase windings. The currents of harmonic orders $12n\pm1$ (n=0,1,2,…) appear in α–β subspace, whereas currents of the orders $6n\pm1$ (n=1,3,5,…) appear in x-y subspace [34]. Since there is no back-electromotive force in x-y subspace, the currents in x-y subspace are only limited by winding resistance and stator leakage inductance. Therefore, for relatively small magnitudes of voltages in x-y subspace, currents of substantial magnitudes will result.

1.3   Electric Drives with High Acceleration Capability

Short-term overload operation is required in traction, aerospace, and machine tools applications. All-terrain vehicles and military vehicle drivetrains also have special requirements such as hill climbing ability, hard acceleration, and high speed because of their harsh operating conditions [15]. The electromagnetic torque in a motor depends on the current density and flux density. The machines are designed to operate in deep magnetic saturation when supplying peak torque [35].

In [36], a fast acceleration method using a delta-star starter has been used for a

weaving motor drive system. The delta-star switching method achieves high inrush current in order to increase starting torque. At starting, a delta connection is used which applies full line-line voltage across the winding. When the speed reaches the desired value, the motor winding is switched to a star-connection. Switches with higher current rating are used to handle the high starting current, which increases the system cost. Faraday Future has demonstrated full-electric vehicles with competitive 0-60 miles per hour acceleration times. Faraday Future uses a patented drivetrain control software called "Battery Boost Mode" in which the inverter switching frequency is reduced from 10 kHz to 3 kHz to keep the switching device's temperature within acceptable bounds when 25% more motor current is forced during acceleration [37].

Some methods to change torque-speed characteristics of multiphase motors have been reported in literature. One more major advantage of multiphase induction motor (MIM) is that they can achieve a wide range of speed torque variation using pole phase modulation (PPM). PPM is a continuous pole changing technique for MIMs which is achieved by changing the phase of the excitation voltage. PPM can be used to obtain high starting torque from a MIM [38]. But, PPM is possible only with certain slot-pole combinations for a given multiphase motor, which may not be optimal for good steady state performance [38].

To get momentary high torque, more than rated current needs to be supplied to the motor. The motor can be overloaded for brief duration, but the converter cannot be overloaded. Therefore, a drive's peak torque rating is limited due to the maximum junction

9

temperature of its switching device, which limits allowable current through it [39]. This requires the devices to be overrated to increase the drive's peak-torque rating.

1.4 Hardware Development for Wide Bandgap Device-Based Converters

Significant research efforts are reported for designing high performance gate drivers [40] - [45], for analyzing the effects of the parasitic inductance and capacitance on the converter performance [46] - [49], for integrating the gate driver and the SiC MOSFET inside the module to minimize the gate-source parasitic inductance [50], and for designing the SiC MOSFET module and dc link bus bar to achieve a low stray inductance [51]. There are also a few papers that address the complete design of converters with WBG devices [51] - [54]. In [53], an approach based on optimization of the power module, the dc and ac bus structures, the gate driver, and the dc link capacitor bank is presented for a 250 kW all-SiC three-phase inverter.

An inverter can be designed on a printed circuit board (PCB), thus cutting down the cost of expensive dc and ac bus bars. The power rating of such an inverter is limited by the heating of the copper planes caused by currents. In such context, ensuring PCB-level electromagnetic compatibility (EMC) is crucial to maintain the integrity of the measured signals (e.g., line currents in a motor drive). This is especially important in an environment with high di/dt and dv/dt, which is typical for WBG devices. The component selection, PCB layer stack up, and routing strategy are crucial for ensuring EMC in an environment with high dv/dt and di/dt.

To achieve their full efficiency benefits, it is crucial to drive SiC MOSFETs in a way that minimizes conduction and switching losses [55], [56]. The main factors

influencing the switching behavior are the turn-on and turn-off energy of the MOSFET, gate drive current requirements, and Miller effect [55].

Minimizing the parasitic inductance of the commutation loop is crucial because the parasitic inductance causes voltage overshoot during the device turn-off. There is a tradeoff between the voltage overshoot and the achievable *di/dt* because the voltage overshoot should not exceed the rated voltage of the device. The stray inductances of the power module, the dc bus bar, the dc link capacitors, and the high frequency decoupling ceramic capacitors constitute the commutation loop inductance [53].

1.5 Trade-off Between High Switching Frequency and EMI, and Motor Insulation Reliability

To justify the higher cost of WBG devices and fully realize their potential, they must be switched at high speeds, but high switching speeds result in additional EMI. High *dv/dt* excites the capacitive coupling paths in converter, cables and motors, causing substantial CM current to flow and this can damage motor insulation. If a high switching frequency is used, as required for low-inductance motors and high-speed motors, the conducted emissions increase significantly and an EMI mitigation strategy must be implemented to comply with EMC standards. SiC-based power devices enable an order-of-magnitude reduction in switching losses relative to the Si IGBT and diode combination presently dominant at 1200 V. However, this comes at the cost of a 20–30 dB increase in the high-frequency spectral content of the switching waveforms, and a 5-times increase in the *dv/dt* of the inverter output [57]. In motor drives, especially those with long cables between the motor and the drive, the high *dv/dt* created by PWM voltage source inverters

11

(VSIs) creates excessive voltage stress in the insulation of ac motors due to voltage reflection [58]. Bearing currents are caused by high *dv/dt* of WBG devices and CM voltage, and these bearing currents can reduce bearing lifespans. A *dv/dt* filter placed between the drive and the motor can be used to reduce the *dv/dt* at the motor terminals. This allows the inverter to switch at high *dv/dt* to minimize switching losses while avoiding the problems associated with high *dv/dt* in the motor and cable.

1.6   Problem Statement

To get momentary high torque, more than rated current needs to be supplied to the motor. The motor can be overloaded for a brief duration, but converter cannot be overloaded. Therefore, a drive's peak torque rating is limited by the maximum junction temperature of its switching devices, which limits allowable current through it. This requires the devices to be overrated to increase the drive's peak-torque rating.

The harmonics of the orders 3, 5 and 7 appear due to dead-time effect in inverters. For an asymmetrical six-phase motor, these harmonics map into x-y subspaces. Due to the fast rise and fall times of WBG devices, the dead time can be significantly lower than the dead time for Si devices. This will reduce the current in x-y subspace. The high switching frequency capability of WBG devices allows a high-bandwidth current control, which will nullify the currents in x-y subspace. This will eliminate extra controllers required in those subspaces.

The reliability of power converters in an electric drivetrain of a vehicle can be a criterion for the comparison of cooling system designs and various control strategies. Therefore, reliability prediction is important for design and control of vehicles. This

dissertation presents an approach for quantitative evaluation of the reliability of converters for multiphase motor drives for EVs, taking driving cycle into account.

To achieve the maximum benefits from using WBG devices, the converter must be designed with appropriate gate drivers than can switch quickly with minimal overshoot and losses, with minimal parasitic inductance in the commutation loop, and with fast short-circuit protection for the WBG switches. The design considerations to capitalize on the full potential of WBG devices and to ensure PCB level EMC are illustrated in this dissertation.

2. MULTIPHASE DRIVE WITH HIGH TRANSIENT TORQUE CAPABILITY

Electric drives used in electric and hybrid electric vehicles (EVs), electric locomotive traction, electric ship propulsion, more-electric aircraft and industrial electric drives used in weaving machines, conveyors, cargo handling, hoists, printing presses require short-term high torque [59], [60]. To get momentary high torque, more than rated current needs to be supplied to the motor. The motor can be overloaded for a brief duration, but converter cannot be overloaded. The typical torque-speed characteristics and most frequent operating points of a traction motor are shown in Figure 2.1. For quick acceleration, the electric motor is required to deliver high torque at lower speeds. Additionally, hill climbing, reversing at high road gradient and auto-start of the engine also require high torque at lower speeds [59]. The torque requirement for acceleration, passing, and grade ability of Chevrolet Bolt battery electric vehicle is shown in Figure 2.2 [61].

2.1   Short Term Overload Capability of a Motor

To get high transient torque, motor is overdesigned and more cooling effort is required for converter and motor. The temperature rise inside the motor must not be allowed to exceed the rated temperature of insulation during a transient overload. Various recognized temperature classifications of insulation systems for electric machines are: class 105 ℃ (A), class 130 ℃ (B), class 155 ℃ (F), class 180 ℃ (H), class 200 ℃ (N), class 220 ℃ (R), class 240 ℃ (S), class above 240 ℃ (C) [62]. The rated temperature of

insulation should not be exceeded. The motor has sufficient heat capacity, so it can be

briefly overloaded. The time duration limit of maximum torque depends on the thermal
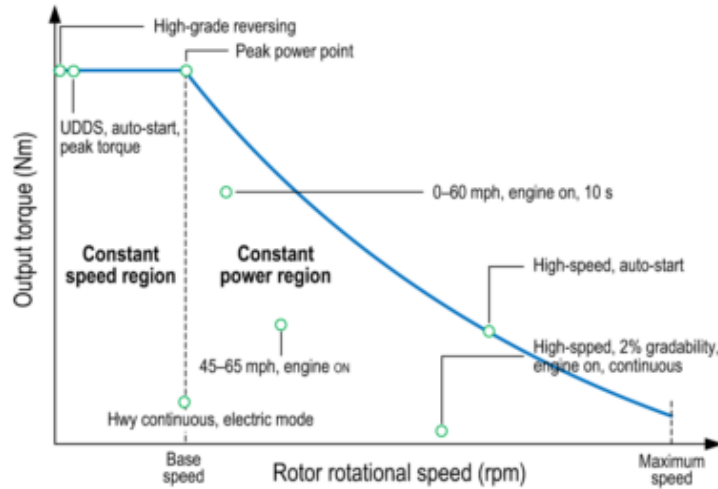
Figure 2.1. Typical torque-speed characteristics and most frequent operating points of an electric vehicle © 2015 IEEE, reprinted with permission from [59].
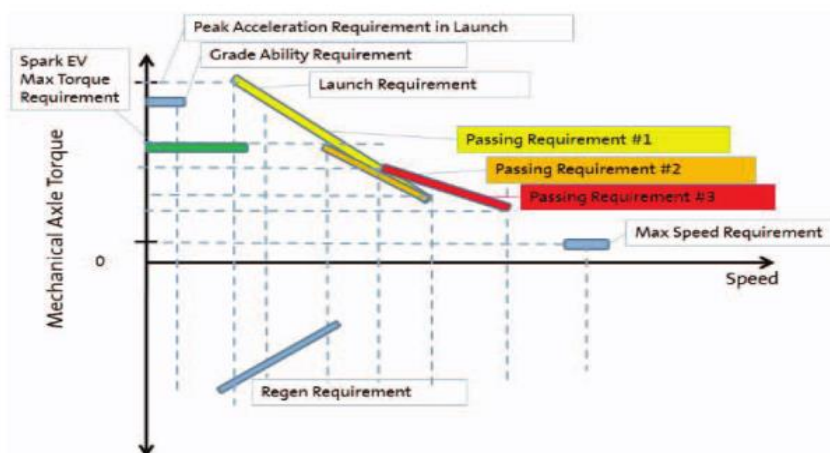
Figure 2.2. Chevrolet Bolt electric vehicle drive unit axle torque requirement © 2017 IEEE, reprinted with permission from [61].

of the motor [63]. The dynamic applications require analysis of transient thermal behavior. The temperature rise characteristic of a stator-limited induction machine can be divided into four modes: subtransient, transition, transient and temperature creep [63]. The first mode is the subtransient regime in which the conductor temperature rises linearly. The maximum temperature rise occurs in this mode for short-term severe overloads because the enamel and insulation have low heat diffusivity. Heat is stored in the conductor's thermal mass. [63]. Therefore, the momentary overload capability of a motor is determined by its subtransient time rating (STR) and associated i^2t rating. The STR is on the order of seconds.

Mode 2 is called transition regime and it starts when the heat reaches the winding surface and starts heating the end space. The maximum temperature rise is reached during transition regime for moderate overloads. Therefore, time ratings for moderate overloads are defined by transition time rating. The third mode transient regime begins when the heat reaches the surface of motor frame and end caps. The time rating in this mode is defined as the transient time rating. The fourth mode is observed during constant current operation.

During subtransient regime, the conductors heat adiabatically due to low thermal diffusivity of the insulation and slot liner. The temperature rise in this mode is given by:

$$\frac{dT}{dt} = \frac{P_{loss}}{C_{th}} \tag{2.1}$$

where P_{loss} is the stator winding loss and C_{th} is the heat capacity of stator conductors. Integrating both sides of (2.1), we get

$$\Delta T(t) = \frac{1}{C_{th}} \int_{t_o}^{t} P_{loss} dt + \Delta T_0 \tag{2.2}$$

16

STR can be found by solving equation 2.2,

$$STR = C_{th} \frac{\Delta T_{max} - \Delta T_0}{P_{loss}} \quad (2.3)$$

where ΔT_0 is the initial temperature rise of the motor and ΔT_{max} is the maximum

allowed temperature rise, which is determined by the insulation class.

To improve the STR, the i^2t rating of the stator conductor should be enhanced. The

approaches are to cool the conductors directly and to allow a higher temperature rise in

the coils by utilizing a higher temperature insulation class for winding insulation. The heat

of the conductors can be removed with cooling channels in hollow conductors which

results in higher heat dissipation and high current capability [64], [65].

2.2   Description of Multiphase Motor Drive with High Transient Torque

Capability

The invention presented here makes it possible to get high transient torque from a

multiphase motor drive at low speeds. This invention is valid for motors with N phases

where N is an even number and greater than or equal to 6. An asymmetrical 6-phase motor,

as shown in Figure 2.3, is used for illustration of the invention. This motor has 2 sets of

3-phase windings (abc and xyz) and these two sets are displaced by 30 degree electrical

angle relative to each other. Legs 1, 3, and 5 of the inverter supply phases a, b and c

respectively and legs 2, 4, and 6 supply phases x, y and z of motor as shown in Figure 2.4.

The motor-inverter system along with all the switches is shown in Figure 2.4. W_A, W_B,

W_C, W_D, W_E, and W_F represent the 6 phase windings. DC+ and DC- represent the dc bus

terminals. The 6 inverter legs are shown separated for ease in illustrating the system

reconfiguration. Six single position double throw (SPDT) switches are represented by

17

SPDT1 to SPDT6. The higher torque can be obtained by converting a 6-phase machine into a 3-phase machine and connecting two inverter legs in parallel with the help of six
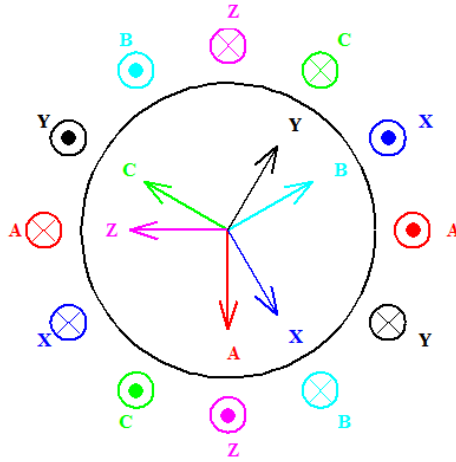
Figure 2.3. Asymmetrical 6-phase motor winding description.

switches. To obtain a 3-phase machine, two adjacent phase windings of a 6-phase machine are connected in series. For example, for the 6-phase symmetrical motor shown in Figure 2.4, we connect phase a in series with phase x, phase b in series with phase y and phase c in series with phase z. Legs 1 and 2, legs 3 and 4, and legs 5 and 6 are connected in parallel. To get high transient torque, up to twice the rated inverter current can be forced at the range of speeds for which the value of back-EMF of the motor is low enough to allow this much current. This current is forced for a duration determined by the STR of the motor, so that the winding temperature remains within the limit imposed by the class of insulation. A super-capacitor can be used to supply this short-duration high current. Table 2.1 shows the contactor position for switching from 6 phase to 3 phase operation and vice versa.

The switchover of the SPDTs occurs during the operation of the electric drive before a transient torque phase. The control circuit deactivates the electric drive currents during the switchover from the 6-phase configuration to the 3-phase configuration and vice versa.
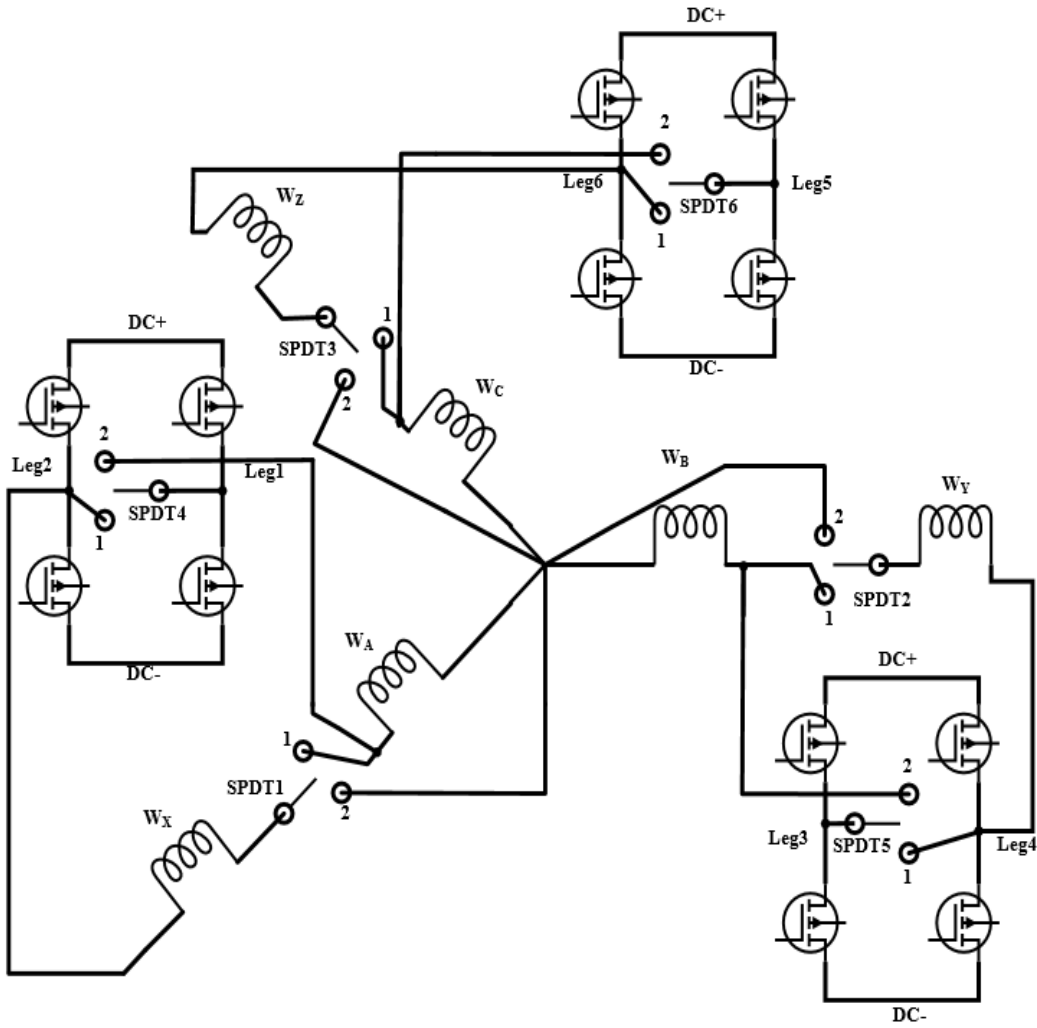
Figure 2.4. Asymmetrical 6-phase motor-inverter system showing all SPDTs.

This ensures that there is no arcing between the contacts of SPDTs and they need to be sized for stationary currents only. During the switchover process, no torque is produced by the electric drive but the interruption is not noticeable due to the inertia of the load. The switchover period can be kept as short as 20-30 ms. The actuator system requires a small setup or lead time to switch the contacts of SPDT. The duration of interruption of the electric drive can be minimized by delaying the deactivation of motor

Table 2.1. SPDT positions for 3 and 6-phase operation of the motor drive.

Mode of operation	SPDT Position					
	SPDT1	SPDT2	SPDT3	SPDT4	SPDT5	SPDT6
3-phase operation	1	1	1	1	1	1
6-phase operation	2	2	2	2	2	2

currents in relation to the actuation system.

2.3   Control of Asymmetrical 6-Phase Induction Motor

$$[T] = \left(\frac{1}{3}\right) \begin{bmatrix} 1 & -\frac{1}{2} & -\frac{1}{2} & \frac{\sqrt{3}}{2} & -\frac{\sqrt{3}}{2} & 0 \\ 0 & \frac{\sqrt{3}}{2} & -\frac{\sqrt{3}}{2} & \frac{1}{2} & \frac{1}{2} & -1 \\ 1 & -\frac{1}{2} & -\frac{1}{2} & -\frac{\sqrt{3}}{2} & \frac{\sqrt{3}}{2} & 0 \\ 0 & -\frac{\sqrt{3}}{2} & \frac{\sqrt{3}}{2} & \frac{1}{2} & \frac{1}{2} & -1 \\ \frac{1}{2} & \frac{1}{2} & \frac{1}{2} & -\frac{1}{2} & -\frac{1}{2} & -\frac{1}{2} \\ \frac{1}{2} & \frac{1}{2} & \frac{1}{2} & \frac{1}{2} & \frac{1}{2} & \frac{1}{2} \end{bmatrix}$$

20

The transformation matrix T is used to convert 6-phase current/voltage variables to $\alpha\beta xy0^+0^-$ components. The $\alpha\beta$ components are then converted to the synchronous frame. The vector space decomposition of multiphase motors is discussed in [66]. The current control methods for different subspaces of multiphase motors are presented in [67]. The parameters for the proportional integral (PI) controllers for the speed and the currents in dq and xy frame of 6-phase motor are selected analytically based on motor parameters and the control loop bandwidths [68], [69].

2.3.1 *Speed Control Using Classical Control Methods*

The parameters of the PI controller for speed are selected analytically as given in [69]. The controller gains are a function of inertia as well as the desired closed loop bandwidth. It has excellent response to reference and load-torque changes. The proportional controller gain is given by:

$$K_p = \alpha_s J \tag{2.4}$$

where J is the total inertia of the motor and the load and α_s is the bandwidth of the closed loop controller. The gain of integral controller is given by:

$$K_i = \left(\frac{\alpha_s}{2\delta}\right)^2 J \tag{2.5}$$

where δ is relative damping. A value of 0.61 was chosen for δ, which gives a phase margin of 60 degrees.

2.3.2 *Current Control Using Classical Control Methods*

The design procedure presented in [69] is used to achieve nearly minimum settling time with negligible overshoot for reference changes. The controller gains are given by:

$$K_p = kL \tag{2.6}$$

21

$$K_i = kR \tag{2.7}$$

where L and R are the transient inductance and resistance of the motor respectively for the $\alpha\beta$ plane and L is the leakage inductance for the xy plane. The optimum value of k is found to be approximately 4% of the angular sampling frequency for the $\alpha\beta$ plane [69] and 10% of the angular sampling frequency for the xy plane.

3. QUANTITATIVE RELIABILITY EVALUATION OF INVERTERS FOR MULTIPHASE MOTOR DRIVES FOR ELECTRIC VEHICLES

3.1 Introduction

Power electronic systems in the drivetrain of an electric vehicle can have adverse effect on the reliability of the vehicle [70]. According to data obtained from field experience, approximately 35% of adjustable speed drive failures are attributed to failure of power electronics [71]. Up to 40% of 3-phase inverter failures in the field are a result of power semiconductors failures [71]. Reliability is the probability that the system will perform the required function without failure under the stated conditions for a specified period of time under given environmental and operational conditions [72]. The inverters used in electric and hybrid electric vehicles (HEVs), wind energy conversion systems and photovoltaic power generation face randomly varying mission profiles [73], [74]. Due to thermal variations, the bond wire and thermal joints of the switching device module can fail. Thermally caused failures constitute a significant percentage of all sources of failures [75]. Quantitative assessment of reliability is important for comparing different topologies, control strategies and components and determining whether the designed system meets the specifications.

In [76], a mission-profile-dependent simulation model based on MATLAB is presented for the quantitative assessment of the reliability of 3-phase motor drive of HEVs. In [72], existing methods to evaluate the reliability of power electronics converters are surveyed. Therefore, multiphase motor drives increase reliability as the motor drive can

still operate with reduced capacity. It is important to quantify the reliability of multiphase motor drives to study the tradeoff between reliability improvement and the cost and complexity added due to the additional phases.

3.2   Reliability Analysis of Power Electronics Systems

Mean time between failure (MTBF) is a widely used performance metric for comparison of various system designs [72]. The MTBF gives the expected average time for which an item operates without failing. A MTBF much longer than the mission duration means that the system is highly reliable within the mission duration. Assuming that the failure rates of components and subsystems are independent of time, reliability can be defined as:

$$\text{Reliability} = e^{-t/\text{MTBF}} \tag{3.1}$$

When the failure rate $\lambda(t)$ is constant , MTBF is the inverse of the failure rate.

The IEC TR 62380 empirical reliability model for IGBTs considers the dormant modes and effects of the temperature cycles on failure rates and includes data from IGBTs. For reliability analysis at the system or sub-system level, the part count model, combinatorial model, and Markov models are used [72]. Among these models, only the Markov models reflect the details of fault-tolerant systems such as the order of component failures, state dependent failure rates, repair process, and reconfiguration.

3.3   Reliability Evaluation Model of Electric Vehicles

In this dissertation, a model is built in MATLAB to evaluate the reliability of the-SiC based inverter for electric vehicles. The block diagram for reliability evaluation is shown in Figure 3.1.

24
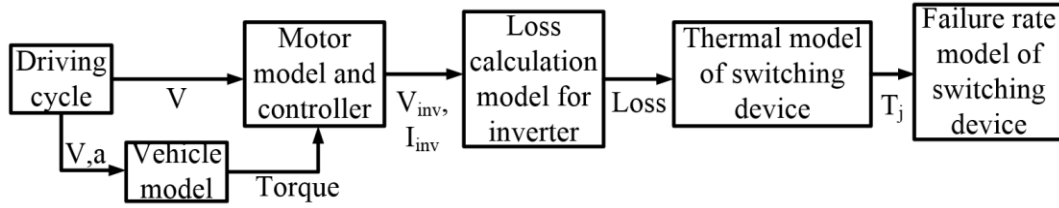
Figure 3.1. Block diagram of the reliability evaluation model.

3.3.1 *Driving Cycle*

A driving cycle consists of standard temporal sequences of vehicle speeds. The driving cycle provides the instantaneous speed and acceleration to the vehicle and motor model. This is used to determine the operating conditions of the inverter in the electric drive. The LA92 driving cycle is used to simulate the driving scenario in this dissertation [77].

3.3.2 *Vehicle Model*

The vehicle speed and acceleration obtained from the driving cycle model are inputs to vehicle model to calculate the instantaneous torque and speed of the traction motor. Parameters of the vehicle, such as vehicle weight, front area, and diameter of the wheels, are obtained from the Toyota Prius. The rolling resistance coefficient, the aerodynamic drag coefficient, and transmission efficiency are obtained from the literature [78]. The vehicle parameters are shown in Table 3.1.

3.3.3 *Motor Model*

The motor model is used to obtain stator voltages and currents using traction torque-speed characteristics obtained from the vehicle model. The motor used is an interior permanent magnet synchronous motor (IPMSM), which is a superior solution for

Table 3.1. Parameters of vehicle.

Parameter	Value
Front area	1.746 m^2
Aerodynamic drag coefficient	0.26
Rolling resistance coefficient	0.01
Transmission efficiency	0.9
Diameter of tire	0.62 m
Number of gears	5
Vehicle mass	1243 Kg

Table 3.2. Parameters of motor.

Parameter	Value
Number of poles	8
Maximum speed	10,000 rpm
Maximum power	70 kW
Maximum torque	185 Nm
Maximum current	176.7 A (rms)
DC-link voltage	360 V
Stator resistance	16.9 mΩ
Permanent magnet flux	0.099 Wb
Nominal d-axis inductance	0.312 mH
Nominal q-axis inductance	0.606 mH

EVs because of its efficiency, power density, and wide speed operating range. In an
IPMSM, torque is determined by both d-axis and q-axis currents. In maximum torque

perampere (MTPA) control, the optimal combination of these two current components is calculated to produce the desired torque while minimizing current magnitude. In the field-weakening region, current minimizing solutions are found at the intersection of the torque and voltage limit curve. The analytical solution to current for MTPA has been obtained in [79] and the same has been used in this dissertation. The EV motor parameters are taken from [79] and shown in Table 3.2. The motor can provide a maximum torque of 185 Nm, which is sufficient for the considered vehicle and driving cycle.

3.3.4   *Post Fault Control of Motor*

Multiphase motor drives have degrees of freedom that can be exploited during post fault operation to control the motor. The two most common optimization criteria for post fault control are minimum-loss mode and maximum-torque mode. In this dissertation, maximum torque mode is used while keeping the post fault currents below the rated value to satisfy thermal limit of the power converter and motor. The detailed procedure to find the post fault currents is described in [80].

3.3.5   *Electro-Thermal Modeling and Loss Model*

For electro-thermal simulations of long driving cycles (about 25 minutes) of EV powertrains, the challenge is achieving fast simulation speeds so that simulations can be conducted within hours. This challenge exists because thermal simulations need a few hours to produce results due to the large thermal time constants of cooling systems. This makes coupled electric-thermal simulations very slow. Thermal models developed at the National Renewable Energy Laboratory show that if copper is used as the fin material with airflow through the micro-channels and the base plate is held at 125 ℃ heat fluxes from
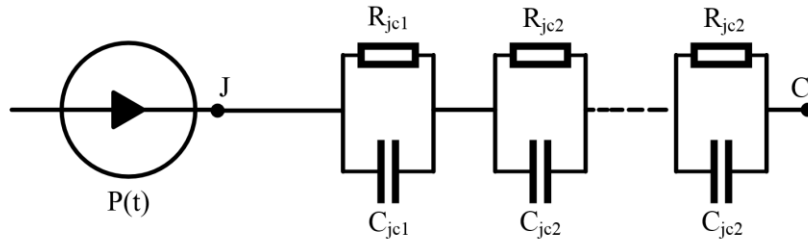
Figure 3.2. Foster model of junction to case thermal impedance.

60 W/cm^2 to 180 W/cm^2 can be dissipated and it is sufficient to keep the device junction temperature within allowed limits [81]. Keeping this cooling technology in mind, the baseplate or heat sink temperature is kept constant at 125 ℃. With the base plate temperature fixed, we can use a simple thermal equivalent circuit for finding the junction temperature of the switching devices and hence avoid a significant computational burden. A complete analytical solution for calculating the losses of switching devices of voltage source inverter (VSIs) is presented in [82]. In these models, the average current and voltage values obtained from the control system of the power converter are used for loss calculations assuming a linear loss model, which uses datasheet information. This works very well for complex power converters like pulse width modulation (PWM) controlled inverters. The loss model used is a good choice for electro-thermal simulations as it has high computational efficiency.

In this dissertation, the partial fraction circuit, also known as Foster model or pi model, is used for the thermal equivalent circuit of the device module, as shown in Figure 3.2 [83], [84]. This circuit is used in datasheets, as the coefficients can be easily extracted from a measured cooling curve of the power switch or module. The partial fraction

28

coefficients are provided in datasheets as thermal resistance and thermal time constant pairs. The partial fraction coefficients are provided in datasheets as thermal resistance (r) and thermal time constant (τ) pairs with $\tau_i = r_i c_i$. The thermal time constant of the SiC device package is of the order of hundreds of milliseconds. The thermal impedance curve can be written as:

$$Z_{thjc}(t) = \sum_{i=1}^{n} r_i * (1 - e^{-t/\tau_i}) \tag{3.2}$$

$$T_j(t) = P(t) * Z_{thjc}(t) + T_{case}(t) \tag{3.3}$$

where P(t) is total loss, $T_j(t)$ is junction temperature, T_{case} is the base plate temperature and Z_{thjc} is the junction to case thermal impedance.

3.3.6 *Failure Rate Model of MOSFET*

The MOSFET failure rate model given in [85] can be expressed as:

$$\lambda_{MOSFET} = (\lambda_{die} + \lambda_{package} + \lambda_{overstress}) * \frac{10^{-9}}{h} \tag{3.4}$$

$$\lambda_{die} = \pi_S * \lambda_0 * \frac{\sum_{i=1}^{y}(\pi_t)_i * \tau_i}{\tau_{on} + \tau_{off}} \tag{3.5}$$

$$\lambda_{package} = (2.75 * 10^{-3} * \sum_{i=1}^{z}(\pi_n)_i * (\Delta T_i)^{0.68}) * \lambda_b \tag{3.6}$$

$$\lambda_{overstress} = \pi_i * \lambda_{EOS} \tag{3.7}$$

where λ_{die} represents the failure rate of the MOSFET die, $\lambda_{package}$ represents the MOSFET package failure rate, which is caused by thermal cycling, and $\lambda_{overstress}$ denotes the effect of overvoltage and overcurrent stress on the component failure rate.

The parameters are further explained as follows.

λ_0 and λ_b are base failure rates of the die and the package respectively.
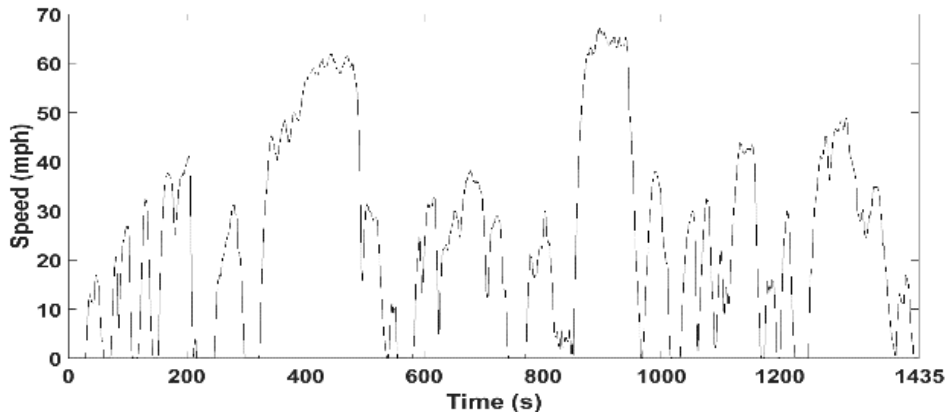
Figure 3.3. LA 92 driving cycle.
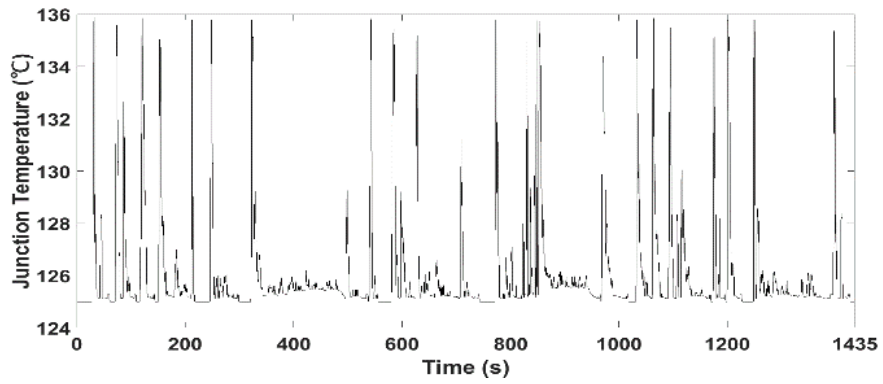
Figure 3.4. Junction temperature of SiC MOSFET for a 6- phase converter in the LA 92 driving cycle.

Π_s denotes the effect of the voltage stresses and is determined by the ratios of the applied collector-to-emitter and gate-to emitter voltages to the corresponding rated voltages. $(\pi_t)_i$ represents the effect of junction temperature on the failure of the die in the ith phase of mission profile.

τ_i is the working time ratio of the MOSFET in the ith phase of the mission profile.

τ_{on} corresponds to the total working time ratio.

30

τ_{off} corresponds to the total dormant time ratio.

τ_i, τ_{on}, and τ_{off}, represent the effect of the dormant mode on the failure of MOSFETs.

$(\Delta T)_i$ is the amplitude of the thermal variation in the ith phase of the mission profile.
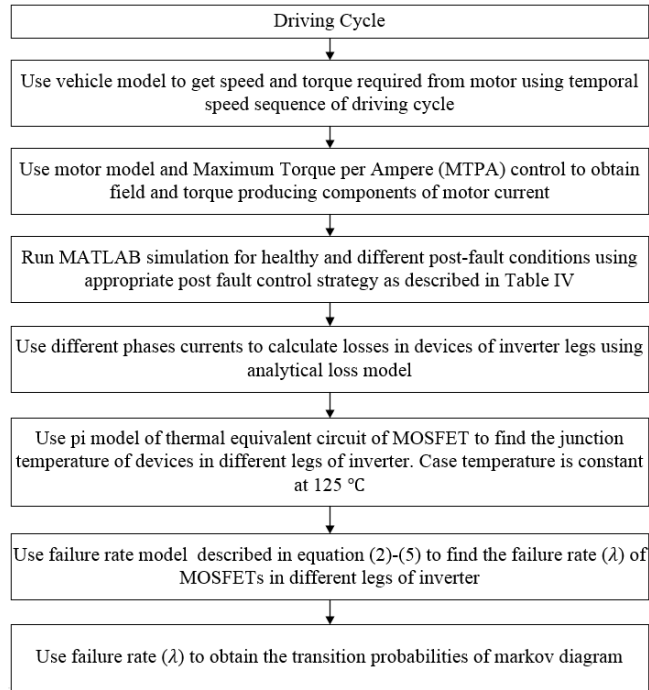
Figure 3.5. Flowchart for the calculation of failure rate.
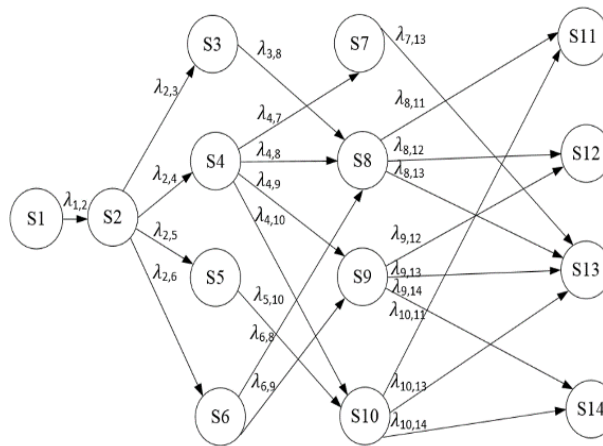
Figure 3.6. Markov model of a 6-phase converter showing states and transitions.

$(\pi_n)_i$ is the factor that takes into account the annual number of thermal cycles seen by the package with the amplitude of $(\Delta T)_i$ The unit of the failure rate in the given equation is the number of failures per billion (10^9) hours.

3.4   Reliability Evaluation and Discussion

Figure 3.3 shows the speed versus time profile of the LA 92 driving cycle. Figure 3.4 shows the junction temperature variation of devices of a 6-phase converter supplying asymmetrical 6-phase motor for LA 92 driving cycle. Figure 3.5 shows the flowchart for the process of quantification of reliability. The Markov model diagram of a 6-phase converter supplying asymmetrical 6-phase motor is shown in Figure 3.6. The Markov model is based on graphical representation of system states that correspond to system configurations, which are reached after a unique sequence of failures and transitions between these states. Table 3.3 describes all the possible post-fault states of asymmetrical 6-phase motor drive used for generating the Markov model. There are 10 post-fault states in which motor drive can operate with reduced performance. The model has 14 states represented by nodes: S1 to S14. S11, S12, S13 and S14 are absorbing states. The transition failure rates as shown in Table 3.4, have been calculated using the method presented in this dissertation. The arrows represent transition between states as a result of component failures. $\lambda_{x,y}$ represents the probability of transition from state x to state y. The Chapman-Kolmogorov equation is used to analyze Markov model. For illustration, the Chapman-Kolmogorov equation for nodes S1 and S2 are given by:

$$\frac{dP_{S1}(t)}{dt} = -\lambda_{1,2}P_{S1}(t) \tag{3.8}$$

$$\frac{dP_{S2}(t)}{dt} = -\left(\lambda_{2,3} + \lambda_{2,4} + \lambda_{2,5} + \lambda_{2,6}\right)P_{S2}(t) + \lambda_{12}P_{S1}(t) \tag{3.9}$$

where $P_{Sk}(t)$ is the probability of system being in state k at time t. The system has 10 non-absorbing states: S1 to S10. Therefore, at time t, the system reliability can be expressed as:

$$R(t)=\sum_{k=1}^{10} P_{Sk}(t) \tag{3.10}$$

Table 3.3. Possible post-fault states of 6-phase motor drive for Markov model.

S.No.	State	Description	Status of phases
1	P6	All phases healthy	All Phases healthy
2	P5_1	5 phases healthy	One of the phases faulty
3	P4_1	4 phases healthy	30° angle between faulty phases
4	P4_2	4 phases healthy	120° angle between faulty phases
5	P4_3	4 phases healthy	150° angle between faulty phases
6	P4_4	4 phases healthy	90° angle between faulty phases
7	P3_1	3 phases healthy	3 phases with 120° angle among them healthy
8	P3_2	3 phases healthy	3 healthy phases with windings at 90° and 120° with first one
9	P3_3	3 phases healthy	3 healthy phases with windings at 120° and 210° with first one
10	P3_4	3 phases healthy	3 healthy phases with windings at 210° and 240° with first one
11	P2_1	2 phases healthy	30° angle between healthy phases
12	P2_2	2 phases healthy	90° angle between healthy phases
13	P2_3	2 phases healthy	120° angle between healthy phases
14	P2_4	2 phases healthy	150° angle between healthy phases

Table 3.4. Transition failure rates in Markov model of the motor drive.

Failure rate	Value (/10^6 hours)
State 1 to 2 ($\lambda_{1,2}$)	1.8000
State 2 to 3 ($\lambda_{2,3}$)	0.2200
State 2 to 4 ($\lambda_{2,4}$)	0.9370
State 2 to 5 ($\lambda_{2,5}$)	0.2500
State 2 to 6 ($\lambda_{2,6}$)	0.8388
State 3 to 8 ($\lambda_{3,8}$)	0.2000
State 4 to 7 ($\lambda_{4,7}$)	0.3200
State 4 to 8 ($\lambda_{4,8}$)	0.2200
State 4 to 9 ($\lambda_{4,9}$)	1.6914
State 4 to 10 ($\lambda_{4,10}$)	1.6922
State 5 to 10 ($\lambda_{5,10}$)	1.6916
State 6 to 8 ($\lambda_{6,8}$)	1.6838
State 6 to 9 ($\lambda_{6,9}$)	1.6838
State 7 to 13 ($\lambda_{7,13}$)	2.2574
State 8 to 11 ($\lambda_{8,11}$)	2.6304
State 8 to 12 ($\lambda_{8,12}$)	0.2424
State 8 to 13 ($\lambda_{8,13}$)	1.2000
State 9 to 12 ($\lambda_{9,12}$)	0.5600
State 9 to 13 ($\lambda_{9,13}$)	2.7946
State 9 to 14 ($\lambda_{9,14}$)	3.2418
State 10 to 11 ($\lambda_{10,11}$)	1.3002
State 10 to 13 ($\lambda_{10,13}$)	10.9962
State 10 to 14 ($\lambda_{10,14}$)	17.9298

4. DESIGN OF INSULATION FOR WBG DEVICE-BASED VOLTAGE SOURCE INVERTER FED MOTORS

4.1 Introduction

Low voltage motors usually have random-wound stators, which consists of round magnet wire, phase separator papers, ground wall insulation, and coil separators. Magnet wire is a wire insulated with an enamel coating on the wire itself. In a random wound motor, each turn can be placed against any other turn, so the word random wound is used. Form wound stators are made of insulated coils that have been pre-formed before insertion into slots. A typical form wound winding is shown in Figure 4.1. It has a continuous loop of rectangular magnet wires shaped into a coil with additional insulation applied over the preformed coils. Several coils with 2 to 12 turns in each coil are connected in series. In form wound stators, each turn in a coil is adjacent to another turn with the smallest possible voltage difference, which makes it possible to have thinner interturn insulation in a coil. In large machines, solid copper bars called Roebel bars are used instead of multi-turn coils and such motors are called form/bar wound. The motors rated for >700 V rms are generally form/bar wound.

Short circuit failure of a motor stator winding due to aging or insulation damage is one of the most prominent causes of motor failure, accounting for 35% of all failures [86]. For optimal design of interturn insulation, it is important to evaluate the electric stress that

the insulation has to withstand and understand the degradation mechanisms of the insulation. Partial discharge is one of the main reasons of premature insulation failure in
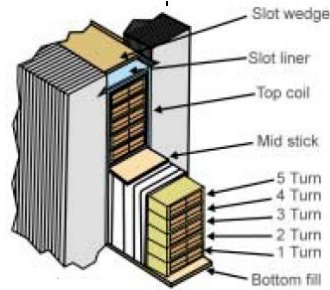
Figure 4.1. A typical form wound coil.

PWM inverter fed motors. The presence of micro-voids inside an insulation is unavoidable. The electric field in these gas filled voids is much higher than the surrounding insulation medium, so the partial discharge can take place, which can cause slow and steady degradation of insulation. The insulation requirements of a PWM converter fed motor is different from that of a grid voltage fed motor.

Due to surge impedance mismatch of the cable and the motor, an overvoltage occurs at the motor terminal due to voltage reflection even if the voltage front is not very steep. In [87], the dependency of the surge impedance of a motor on the system parameters is discussed; the surge impedance varies with motor's power rating and number of parallel paths in the winding. A high power motor has lower surge impedance. Therefore, the overvoltage due to reflection is less for a given cable. If the voltage at the motor terminal of a PWM VSI drive has a steep front, the voltage distribution is non-uniform among the coils of a winding and among the turns of a coil [88]. In [89], the transient voltage distribution in windings of PWM VSI fed motor is modelled. The degree of non-

uniformity depends on the rise-time of the voltage at the motor terminals and the winding or coil-design parameters. In [90], a multi-conductor lossy transmission line model has been used to analyze the voltage distribution in a motor winding subjected to a steep fronted voltage. A time-domain equivalent circuit is used to represent a multi-conductor line, which takes into account the effect of wave propagation and reflection.

In [91], the reflected wave phenomenon in motor drives using WBG devices is discussed. The maximum cable length that produces a given voltage overshoot decreases as the voltage front becomes steeper. In [92], the effect of PWM VSI on the voltage distribution among the turns and coils of a random wound induction motor is simulated using the high frequency distributed-circuit parameters of motor estimated by finite-element method.

The dimensions of motor windings become comparable to the wavelength of associated electromagnetic field for a fast rise time of 20-100 ns. Therefore, the motor terminal voltage is given by the superposition of the forward travelling wave and the reflected wave, and it can even reach more than double the applied voltage. The same phenomenon also happens in a winding. The winding capacitance gets charged by the voltage wave. Standard resin and mica based insulation, used for form wound windings, have a relative permittivity equal to 4. The speed of the voltage wave traveling in a winding can be determined by

$$V_{winding} = \frac{c}{\sqrt{\epsilon_r}} \tag{4.1}$$

where c is the speed of light and ϵ_r is the relative permittivity of the medium. The wavelength λ can then be calculated from the speed of the traveling wave using:
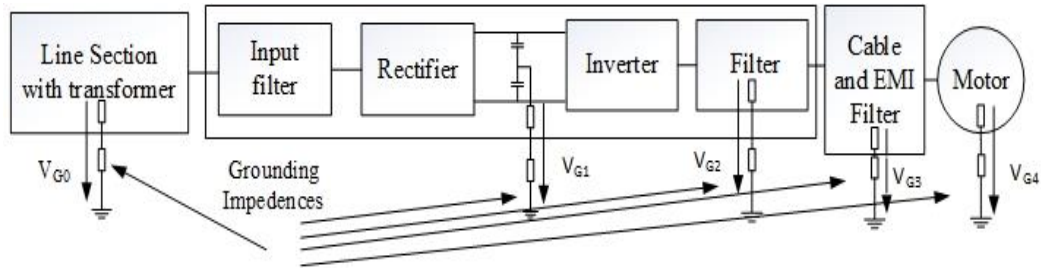
Figure 4.2. Components of an electric drive and grounding of the components [93].

$$\lambda = (V_{winding}/f_{max}) \tag{4.2}$$

where f_{max} is the maximum frequency of the input signal. For a PWM VSI, the maximum frequency is given by:

$$f_{max} = 1/(t_{rise}) \tag{4.3}$$

where t_{rise} is the rise time of the voltage impulse at the motor terminals. For a rise time of 50 ns, the shortest wavelength of the travelling wave is 7.5 m. Generally, the voltage distribution inside a winding can be assumed to be uniformly distributed for a length less than 1/10 of the wavelength. Therefore, for 50 ns rise time, the voltage distribution will be uniform for a maximum winding length of 0.75 m. The cable starts behaving like a transmission line at smaller lengths for fast switching transitions.

4.2 Machine Terminal Voltage Arising from Converter Operation

Figure 4.2 shows the components of an electric drive installation and grounding of the components. The voltage appearing at the terminals of a converter fed machine can be estimated using international electrotechnical commission (IEC) TS 61800-8 and depends on several properties of the electric drive and power distribution system [93]. This standard sets the guidelines for determination of the line-line and phase-ground voltages

at the converter and the motor terminals. The inverter output voltage can be divided into common mode and differential mode. The relationship between parameters like peak value, rise time etc. of input and output voltages of different sections of electric drive are obtained using suitable gains in common mode and differential mode circuits. The amplitude and rise time of voltage at the machine terminals depends on the grounding system, the cable connecting motor and inverter, the machine surge impedance and the presence of any filters that increase the rise time. The connection to ground using a cable is called low frequency grounding. To specify the dynamic voltage behavior in the system, the high frequency grounding performance and topology must also be considered.

In Figure 4.2, V_{G0} to V_{G4} are the grounding potentials of different sections that can be the same or different than the low frequency based grounding potential. Single point grounding has poor high frequency grounding performance as compared to multi-point or mesh type grounding. In the case of single point grounding, the V_{G0} to V_{G4} may contain additional parasitic voltages. The instantaneous values of grounding potential is affected by the configuration of drive and the switching state of the active rectifier and inverter.

The rise time and overshoot of the line-line and line-ground voltage is determined by the switching state of inverter and the snubber circuit of the switching device. In this dissertation, we do not consider any dv/dt filter to prevent insulation damage due to high dv/dt because they add size and cost to the drive and increase losses. Instead, the motor insulation system is boosted. A tradeoff study comparing using a dv/dt filter versus boosting insulation is out of scope of this dissertation; this dissertation focuses on presenting the factors affecting insulation stress and designing the optimal insulation.

The maximum line-line voltage at the motor input can be calculated as:

$$V_{ll\_max,motor} = V_S * \prod_{i=1}^{4} k_{Di} \tag{4.4}$$

The maximum line- ground voltage at the motor input can be calculated as:

$$V_{lg\_max,motor} = \frac{V_{ll\_max,motor}}{\sqrt{3}} + V_{G4\_max} \tag{4.5}$$

where $V_{G4\_max} = V_S * (\sum_{i=0}^{2} k_{Ci}) * \prod_{i=3}^{4} k_{Ci}$

K_{Di} and K_{Ci} are differential mode factors and common mode factors of individual sections.

V_s is the line-line voltage at the input line section as shown in Figure 4.2. In general, the dc link voltage of the active line side rectifier is designed to be at least 5% to 10% higher than the peak line-line voltage. Therefore, the dc link voltage is given by:

$$V_{dc} = 1.1 * \sqrt{2} * V_s = 1.56 * V_s \tag{4.6}$$

The voltage at the inverter ground terminal is either $V_{dc}/2$ or $-V_{dc}/2$ with reference to the mid-point of the dc link. For a cable with cable characteristic capacitance (C_0) and cable characteristic inductance (L_0), the voltage pulse velocity is given by:

$$V = \frac{1}{\sqrt{L_0 * C_0}} \tag{4.7}$$

Critical cable length is defined as the cable length travelled when a voltage pulse travelling along the motor cable, returns to power converter after being reflected at the motor. Critical cable length is given by:

$$l_{cr} = \frac{V * t_r}{2} \tag{4.8}$$

where t_r is the rise time. The reflection coefficient depending on the impedance mismatch between the motor and the cable is given by:

$$T = \frac{Z_m - Z_0}{Z_m + Z_0} \tag{4.9}$$

where Z_0 is the cable characteristic impedance and Z_m is the motor surge impedance. The motor surge impedance is not readily available and difficult to measure. Some typical values of motor surge impedance and reflection coefficient are given in Table 4.1. High frequency EMI filters are only used as common mode filters to reduce the conducted and radiated emissions. The target frequency range is from 150 kHz to 100 MHz. Therefore, EMI filters do not affect the insulation design. EMI filters are often used at the input terminals of the electric drive and at the inverter output also in some applications. The common mode and differential mode gain factors for a cable are given in Table 4.2. The common mode and differential mode gain factors for the considered electric drive installation with an active rectifier are given in Table 4.3.

4.3   Motor Insulation

The most common insulating materials in electric machines are mica, polyester films, aramid paper, epoxy or polyester resins. Insulation can be divided into two categories: groundwall and conductor. Conductor insulation separates the wires and turns

Table 4.1. Typical surge impedance and reflection coefficient of a motor.

Motor power (kW)	Surge impedance (Ω)	Reflection coefficient
< 3.7	2000-5000	0.95
90	800	0.82
355	400	0.6

Table 4.2. Cable section gains based on cable length.

Factors	Cable length < Critical cable length	Cable length > Critical cable length
Differential mode factor (Kd4)	$\dfrac{l_C * T}{l_{Cr}} + 1$	1+T
Common mode factor (Kc4)	$\dfrac{l_C * T}{l_{Cr}} + 1$	1+T

Table 4.3. Gains of different sections of motor drive.

Factors	Input rectifier section	Inverter section	EMI filter section	Cabling and motor section
Differential mode factors	Kd1=1.56	Kd1=1	Kd1=1	Kd1=1.95
Common mode factors	Kc1=0	Kc1=+/- 0.5	Kc1=1	Kc1=1.95

of a coil. Groundwall insulation galvanically separates the coil from the iron core of machine. The main insulations are slot insulation and phase-phase insulation in the slot and the coil end. A polyester film is suitable for slot insulation. If two layers are used, aramid paper is used for the inner layer as it has better thermal resistance. In phase-phase spacing, flexible, cloth like insulation is used for end windings. For high voltage applications, mica is used. Insulation of the conductor is the most demanding task as it is closest to the hot copper wire and the thinnest insulation component. The most common conductor varnishes used in machines are amide-imides. Polyamide-imide is one popular option. The varnish can have several layers. According to the thickness of their coating, magnet wires can be divided into three grades: Single (Grade 1), double (Grade 2), triple

(Grade 3). Polyimide films and aramid papers can also be used as conductor insulation which are wrapped on a wire like tape. However, they are expensive, so they are only used for extremely harsh environments. For high voltage machines, above 6 kV, there is also a conductive corona protection between the insulation and slot wall. The purpose is to prevent partial discharge in voids. IEC standards describe the qualification and quality control test of the insulation of type I [94] and type II [95] rotating electric machines fed from VSI.

4.4   Factors Affecting Inter-turn Insulation

The peak line to line voltage ($\hat{V}_{PP}$) of a two level inverter is called the jump voltage. The pulse repetition frequency (f_P) is the same as the switching frequency (f_{sw}) for a two level inverter. The jump voltage ($\hat{V}_{PP}$) occurs at both the rising and falling edges of the phase-ground voltage.

The voltage overshoot is created by reflected waves at the interface between the cable and the machine terminals due to impedance mismatch. The jump voltage at the impulse repetition rate is important in defining the voltage enhancement that can occur across the first few coils in a winding. The voltage enhancement is a function of rise time and cable length. Voltages above $2V_{dc}$ can be produced by double transitions and also if a minimum time is not allowed between successive pulses in PWM. Double transition/jump occurs when two phases switch simultaneously and has to be avoided by control. If the time between two impulses is matched with the time constant of the cable between inverter and machine, an overvoltage greater than $2V_{dc}$ can appear at the machine terminals. Voltage stress on the interturn insulation is determined by the amplitude and rise time of

43

the jump voltage of the phase-ground, the type of winding, number of coils and the number and length of turns.

4.5 Form Wound Motor with Minimum Inter-turn Insulation Stress

In random wound stator windings (also called mush windings), the position of each turn inside the slot varies randomly, making it impossible to determine the exact winding parameters like interturn capacitances and mutual inductances. Therefore, the insulation of a machine is often designed based on the worst-case scenario that is typically a neighboring location of the first and last turn of the coil. For bar wound or form wound windings, the location with respect to the other turns of the coil inside the stator slot is fixed and precisely known. This makes it possible to determine the exact values of the winding parameters and allows an easier optimization of the coil insulation system to withstand the fast transient voltages created by PWM VSI. In traction applications, bar-wound construction improves the motor performance, especially in the low to medium speed range. [61]. High conductor fill for the same slot area, reduced effective thermal resistance between the copper bar, the laminations and reduction in cost due to easier assembly and decreased copper wire insulation costs are the main inherent advantages of bar-wound stators. In [61], the design of bar wound motor for Chevrolet Bolt electric vehicle has been described. Winding layout is optimized to minimize voltage between conductors within the slot, which increases slot fill factor by allowing minimum insulation between conductors.

4.6   Calculation of Electrical Stress on Different Insulations in a Motor

The voltages for which different motor insulations must be designed and tested are

given by:

Table 4.4 Value of parameters for insulation design.

Insulation	PD safety factor	Temperature factor	Ageing factor
Phase/Phase	1.25	1.3	1.2
Phase/Ground	1.25	1.1	1.2
Interturn	1.25	1.3	1.2

$$\text{Phase} - \text{phase voltage} = (V_{dc} + 2 * V_{InverterOvershoot}) * K_{Ageing} * K_{PDSafe} * K_{PDTemperature} \tag{4.10}$$

$$\text{Phase} - \text{ground voltage} = 0.7 * (V_{dc} + V_{InverterOvershoot}) * K_{Ageing} * K_{PDSafe} * K_{PDTemperature} \tag{4.11}$$

$$\text{Interturn voltage} = (V_{dc} + 2 * V_{InverterOvershoot}) * K_{dv/dt} * K_{Ageing} * K_{PDSafe} * K_{PDTemperature} \tag{4.12}$$

The worst case values for the parameters are given in Table 4.4.

$V_{InverterOvershoot}$ is the overshoot in the voltage at motor terminals and depends on rise time

and cable length. K_{Ageing} takes the thermal aging of insulation into account. The ageing

factor depends on the service temperature and the temperature class of the insulation.

K_{PDSafe} is to take into account the factor by which the PD test voltage should be increased.

An increase in winding temperature from 25 °C to 155 °C typically causes the partial

discharge inception voltage to fall by 30%. $K_{dv/dt}$ takes into account the non-uniform

voltage distribution due to fast rise time. For a random wound motor with a rise time of

50 ns at the motor terminals, 90% of the jump voltage can occur as inter-turn voltage in the worst case [96]. Therefore, $K_{dv/dt}$ for a random wound motor is 0.9. For a form wound motor, the voltage distribution is found among the coils of a winding and turns of a coil and is used for voltage stress calculation.

4.7   Advantages of High Voltage Motors

Along with the recent technological advances in motors, SiC devices are enabling the next generation of high-speed, direct-drive Medium-Voltage (MV) drives for MW class motors in a wide variety of critical energy applications [97]. Higher voltage means lower current, so smaller conductors can be used to feed motors. The efficiency of a medium voltage (MV) motor may be lower than that of a low voltage (LV) motor because of lower slot-fill, but lower currents reduce the stress and heating on electrical distribution system which increases reliability. Form/bar wound coils for MV motors require more insulation. Therefore, larger slots are required in MV motor designs as compared to LV motor designs. The cost comparison of high voltage and low voltage electric drives depends on many factors. Typically, the largest impact on cost is the reduced size of conductors at high voltage. If feeders to distribution equipment or motors in the field are long, the cost savings will be much higher. Generally, the cost of the distribution system outweighs the small difference in the efficiency of motor. One example of very high-voltage motor is ABB's 40 kV synchronous motor driving a compressor at an air separation plant in Sweden [98]. This 6.5 MW motor connects directly to a 42 kV bus without an intervening transformer and dramatically cuts the plant's energy losses.

4.8   Investigation of the Voltage Distribution in Form Wound Windings Due to

Steep-Fronted Voltage

The voltage distribution is simulated using an equivalent π-section lumped circuit model based on parameters determined by finite element method (FEM). This model is found to have a close agreement with the experimental voltage distribution results [99]. The most recommended model for studying voltage distribution in winding is the multi-conductor transmission line (MTL) model, which takes into account the mutual inductance between turns. Equivalent resistor-inductor-capacitor (RLC) circuits are used to represent the turns of the coils of a winding. The stator winding of each phase has several phase groups and each phase group consists of several coils connected in series. Each turn is made of a number of conductors and preformed. The number of turns and the conductor area obtained from MATLAB code are used in simulations. A 2-D FEM model is built up based on the winding configuration. Magnetic steady state FEM is used to determine the self- and mutual-inductance and resistance in each turn of the coil. Electrostatic 2-D FEM simulation is used to find the capacitances between the winding turns and the turn and the grounded stator. The frequency of the simulation is determined from the voltage step rise time. For simplicity, it has been assumed that the location of turn near the slot wedge or near the stator yoke does not influence the parameters. The interaction of different phases is neglected. It is assumed that all coils have the same parameters irrespective of their position in the series winding connection. Figure 4.3 and Figure 4.4 show the copper fill factor for random wound and form wound motors respectively. The copper fill factor of a slot has been defined as the volume of copper divided by the combined volume of copper

and inter-turn insulation. The copper fill factor shown here is for the slot in which the first

coil is located, as this will determine the area of the slot required for the motor.
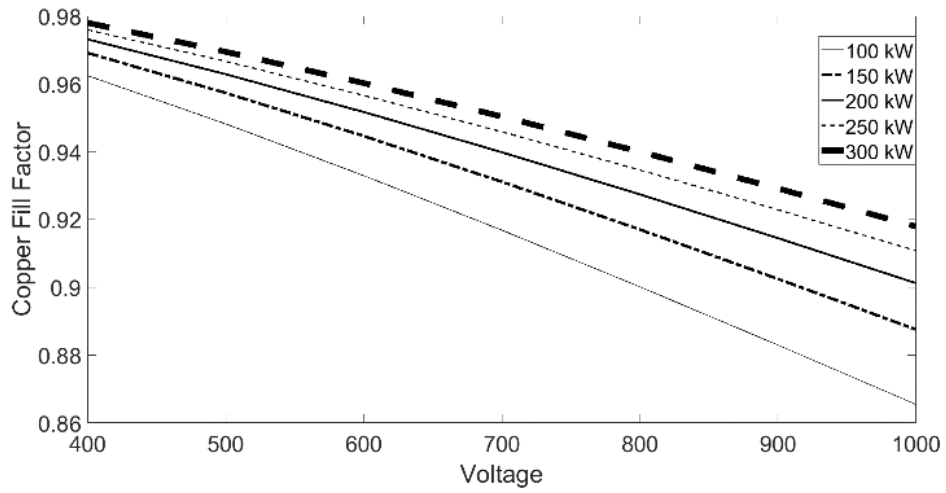
Figure 4.3. Copper fill factor for a random wound motor.
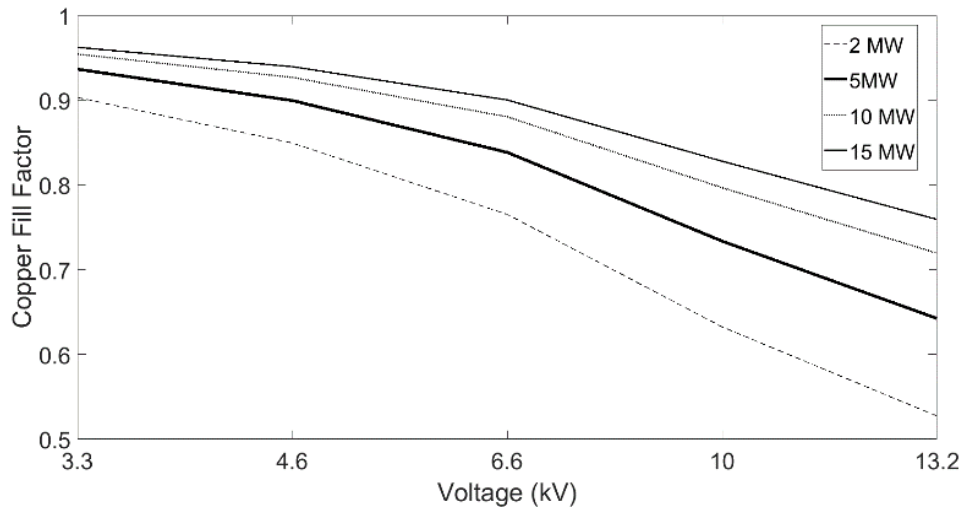
Figure 4.4. Copper fill factor for a form wound motor.

5. HARDWARE DEVELOPMENT FOR WIDE BANDGAP DEVICES

This chapter presents the design of SiC and GaN-based multiphase inverters. To extract maximum performance from WBG devices and minimize electromagnetic interference, hardware needs to be designed in a specific way. The main aspects influencing the switching behavior are the turn-on and turn-off energy of the MOSFET, gate drive current requirements, and the Miller effect.

5.1   Gate Driver Design Considerations

To achieve their full efficiency benefits, it is crucial to drive WBG devices in a way that minimizes conduction and switching losses [100]. A good gate driver must decrease the switching power losses, have protection features, and be electromagnetically compatible. The main aspects influencing switching behavior are the dependence of turn-on and turn-off energy of the switching device on the gate resistance, gate drive current requirements, and Miller effect [101]. The peak gate current available during the switching transient is critical in achieving rapid switching transitions [101], [102]. Preventing gate voltage overshoot and ringing following a switching transition is necessary to ensure reliability of the gate insulation [102]. The parasitic inductance of the gate-source loop needs to be minimized because there is a trade-off between the gate voltage overshoot and the switching speed [102].

The gate driver integrated circuit (IC) used to drive the high side switch in a half bridge configuration must have a high CM transient immunity (CMTI). The CMTI is defined as the maximum slew rate of voltage between two isolated grounds. Insufficient

CMTI can cause malfunction of the gate driver. The CM current injection in the control circuit through the coupling capacitor of an isolated power supply or through the parasitic capacitance of the isolation in gate driver IC can corrupt control signals on primary side. Isolated power supplies with coupling capacitance as low as few pF are available, which ensures high *dv/dt* noise immunity. The CM current can be minimized by using a CM choke if the coupling capacitor is not small [52].

SiC MOSFETs and GaN high electron mobility transistors (HEMTs) have relatively low gate-source threshold voltages of around 2.5 V and 1.3 V, respectively, which decrease with the junction temperature [103]. These low threshold voltages make them immune to *dv/dt* noise [104]. Therefore, it is crucial to design the gate driver circuit with low impedance. The fast switching can cause high *dv/dt,* which causes displacement current to flow through the Miller capacitance of the power switch and can lead to an unintended dynamic turn-on of the switch in the off-state in a half-bridge configuration [103]. This is called the Miller effect or crosstalk. A Miller clamp circuit can sink the Miller current across a low impedance path in a high *dv/dt* situation. If the gate driver IC does not have an active Miller clamp feature, an optimum ratio of turn-on and turn-off path resistances and the use of a negative supply voltage during turn-off can provide protection against spurious turn-on.

The high *di/dt* and *dv/dt* in WBG devices can cause very high voltage overshoot and oscillations due to the presence of parasitic inductance in the converter layout and any parasitic capacitance in the load [105], [106].
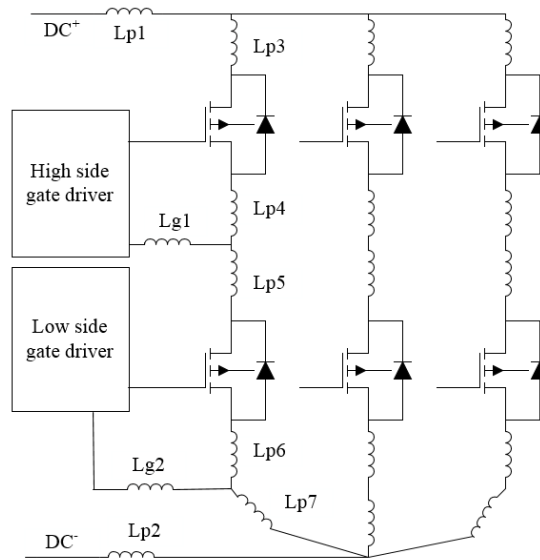
Figure 5.1. Parasitic inductances in a 3-phase inverter layout.

5.2   Power Circuit Design Considerations

The stray inductances of the power module, the dc bus bar, the dc link capacitors, and the high frequency decoupling ceramic capacitors constitute the commutation loop inductance [107]. As shown in Figure 5.1, the inductances Lp1 to Lp7 constitute the stray inductances of the power module and are optimized by the device manufacturer. Stray inductances in the dc side of the loop, Lp1 and Lp2, should reduce the commutation loop inductance. The Lp1 and Lp2 inductances can be minimized by using the dc bus bar, the dc link capacitors, and the high frequency decoupling ceramic capacitors with minimum equivalent series inductance (ESL). If discrete devices are used, then it is the responsibility of the designer to minimize the interconnection inductances of the devices. Minimizing the parasitic inductance of the commutation loop is crucial because the parasitic inductance causes voltage overshoot during the device turn-off. There is a tradeoff

51

between the voltage overshoot and the achievable *di/dt* because the voltage overshoot should not exceed the rated voltage of the device.

Cost, voltage-blocking capability as a function of temperature, capacitance stability as a function of temperature and voltage, root mean square (rms) ripple current capability, reliability, life expectancy, footprint, volume, weight, equivalent series resistance (ESR), ESL, and thermal resistance from hotspot to case each influence the selection of the optimal dc-link capacitor [107]. Film capacitors have best overall performance except that their capacitance per unit volume is small [107]. For electrolytic capacitors, the limiting factor for the dc link capacitors is the rms current ripple requirement because electrolytic capacitors have relatively high ESR, requiring the parallel connection of many capacitors [108]. However, for film capacitors, the determining factor is the capacitance required for the voltage ripple requirements because film capacitors have a low ESR [108]. For film capacitors, the required capacitance decreases as the switching frequency increases up to an optimal frequency where the capacitance cannot be reduced any further due to the rms current rating requirement. This optimal frequency can be as high as 100 kHz, as simulated in [108]. Thus, the high switching frequencies of WBG devices can result in a smaller dc link film capacitor than that required with Si devices.

5.3   Description of the Designed SiC and GaN Inverters

Figure 5.2 shows the designed 4-layer SiC inverter PCB. A two-level inverter has been designed for a motor drive with a 400V dc-link voltage and 20A line currents. The main components are the inverter legs, gate driver circuit, dc link capacitors, hall current

Table 5.1. Main components of SiC inverter.

Component	Manufacturer Part Number
SiC MOSFET	Cree C3M0120090D
SiC Schottky diode	Cree C3D16065A
Gate driver	Infineon 1EDI40I12AHXUMA1
DC link film capacitor	Panasonic EZP-E50117MTA
Gate drive isolated supply	Murata MGJ2D121505SC
Current sensor	LEM LTS 25-NP

Table 5.2. SiC MOSFET datasheet parameters.

Parameter	Value	Units
Rated drain-source voltage, V_{DS}	900	V
Continuous drain current at 25 ℃ case temperature	23	A
Maximum junction temperature	150	℃
On state resistance	120	mΩ
Junction-to-case thermal resistance	1.3	℃/W

sensors, and associated signal-processing circuit. There are 8 inverter legs on this PCB so that it is able to drive multiphase motors. The PCB is a 4-layer PCB. The gate-driver and the power circuits are on the same PCB. SiC MOSFETs in TO-247-3 packages and anti-parallel SiC Schottky diodes in TO-220-2 packages are used. Table 5.1 shows the part numbers of the main components in the SiC inverter. Table 5.2 shows the most important parameters of the SiC MOSFET. Figure 5.3 shows the PCB layer stack-up. The outputs of the Hall current sensors are voltage signals proportional to the current, so they are very

sensitive to noise. Therefore, the outputs of the Hall current sensors and the analog grounds are routed on the top layer so that the ground plane on the first internal layer provides protection from switching noise. As shown in Figure 5.4 and Figure 5.5, the power ground plane is routed on the first internal layer, and the positive dc bus plane and power tracks are on the second internal layer and bottom layer. There is a power ground plane beneath the entire positive dc bus plane, as shown in Figure 5.4 (b) and Figure 5.5 (a). Having positive and negative planes of the dc bus on two consecutive layers of the PCB minimizes the dc link inductance. A similar layer stackup strategy is used for the GaN inverter.
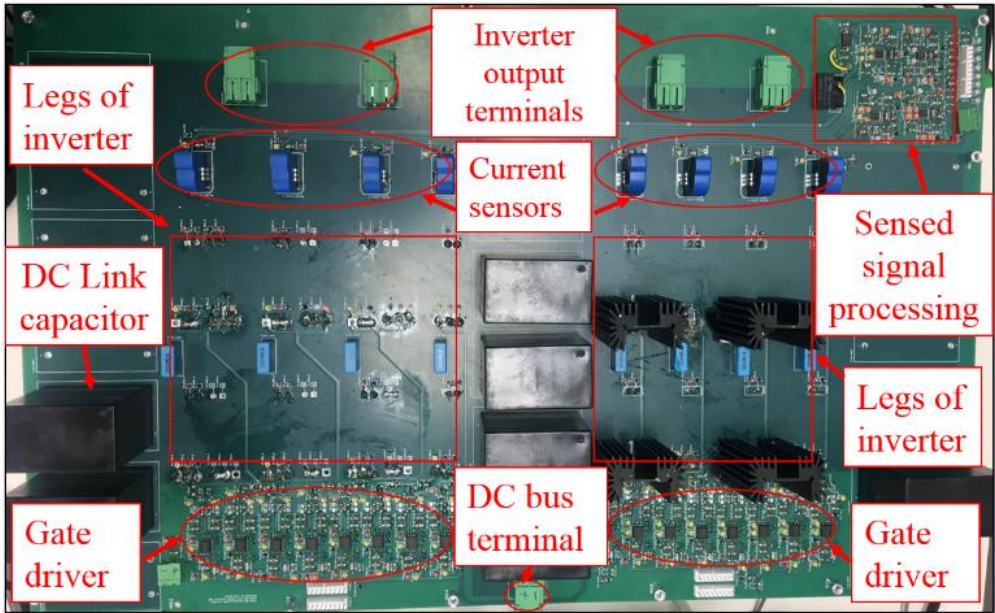
Figure 5.2. 8-phase SiC inverter PCB showing important components.

Sensitive signal layer (Top layer)

Power ground layer (First internal layer)

Power layer (Second internal layer)

Signal layer/Power layer (Bottom layer)

Figure 5.3. PCB layer stackup.

(a)   (b)
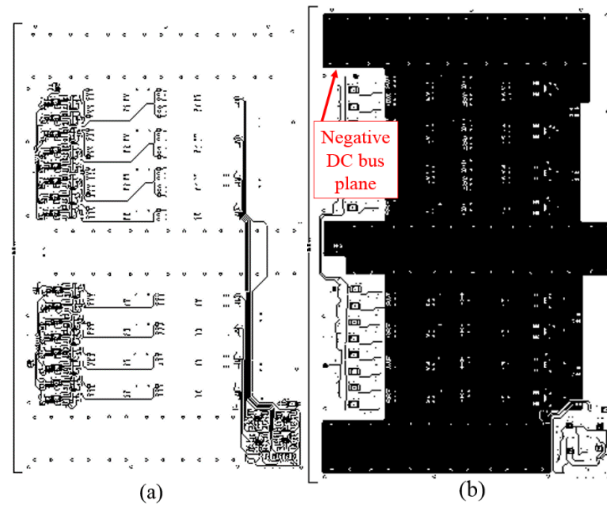
Figure 5.4. Routing on (a) top and (b) first internal layer of the PCB.

(a)   (b)
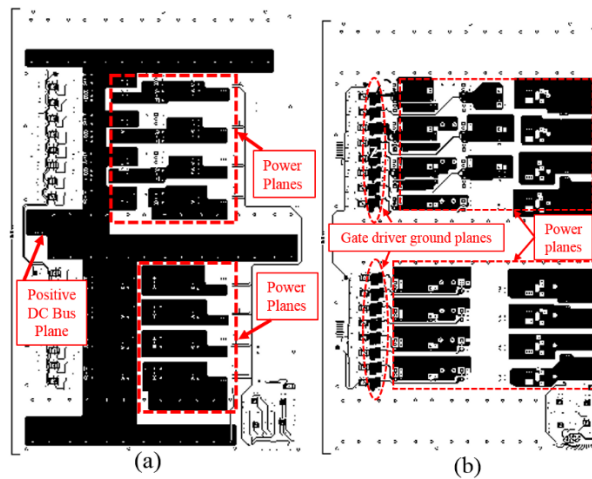
Figure 5.5. Routing on (a) second internal layer and (b) bottom layer.

55

In the designed SiC MOSFET and GaN inverters, separate turn-on and turn-off paths and a negative gate bias voltage are adopted during the off time. The negative gate bias voltage helps in overcoming the Miller effect and reducing the turn-off energy. Therefore, a negative bias voltage of -5 V is used for SiC and -3 V is used for GaN. In the designed PCB, there is a ground plane on the bottom layer beneath all of the gate signal tracks, as shown in Figure 5.5 (b) for the designed SiC inverter, which minimizes the inductance of the gate-source circuit. Minimizing the area of the gate-source loop also makes it less susceptible to the surrounding noise.

The 1EDI40I12AHXUMA1 gate driver IC from Infineon Technologies, which has peak source and sink capabilities of 10A and 9.4 A, respectively, is used to drive the SiC MOSFETs. This gate driver IC has a CMTI of 100 kV/us. The SI8271AB-IS gate driver IC from Silicon Labs, which has peak source and sink capabilities of 1.8 A and 4 A, respectively, is used to drive the GaN transistors. This gate driver IC has a CMTI of 200 kV/µs. The selection of this IC for GaN was driven by its under voltage lockout threshold, considering that the gate drive voltage for GaN is +6 V/-3 V. Both gate driver ICs separate paths for turn-on and turn-off, and can be supplied with a bipolar voltage supply, so a negative gate bias voltage can be used during off time. The MGJ2D121505SC isolated supply from Murata Power Solutions has been used to supply the gate driver for the SiC MOSFETs with a bipolar voltage of +15 V/-5 V. This power supply has an extremely small isolation capacitance of 2.9 pF, which ensures high dv/dt noise immunity. The R05P209S isolated power supply from Recom Power has been used for the GaN gate driver. The 9 V output of this supply is split into +6 V and -3 V supply externally. The
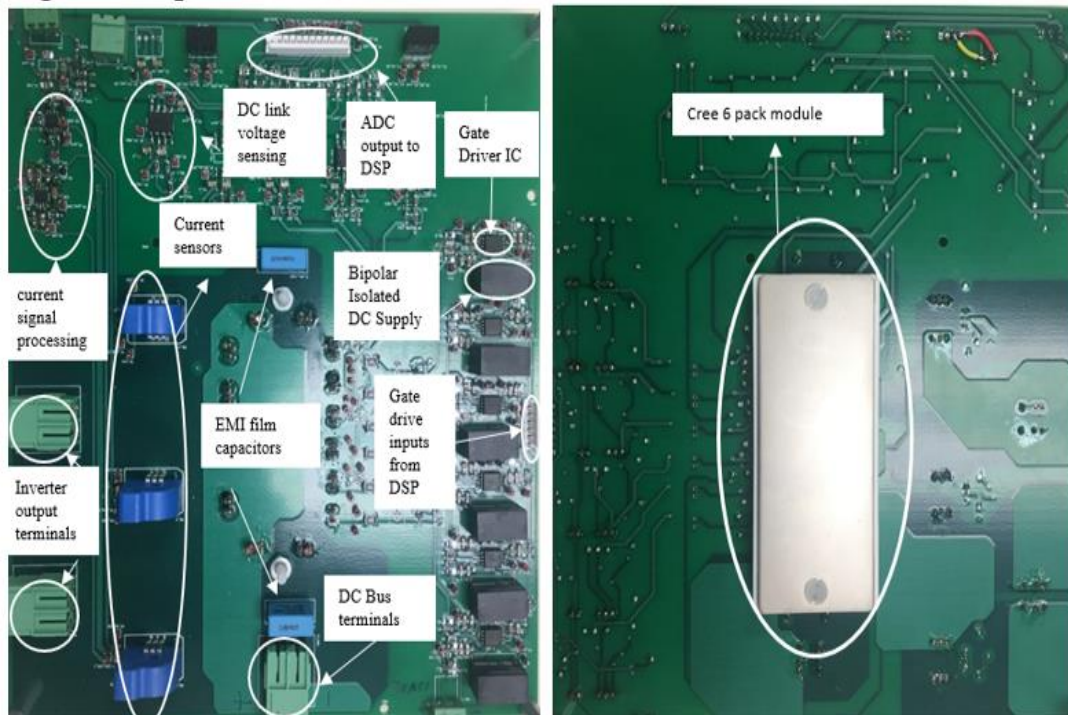
Figure 5.6. SiC-based 3-phase motor drive using 3-phase module from Wolfspeed (Top and bottom view).

RxxP2xx series of power supply has a very low isolation capacitance in the range of 1.5 pF to 10 pF.

A SiC-based 3-phase motor drive was also developed using CCS050M12CM2. The top and bottom view of the PCB is shown in Figure 5.6. Figure 5.7 shows the 6-pack module from Cree, which has a stray inductance of 30 nH between dc bus terminals. The recommended gate-source voltage for this module is +20 V/-5 V.
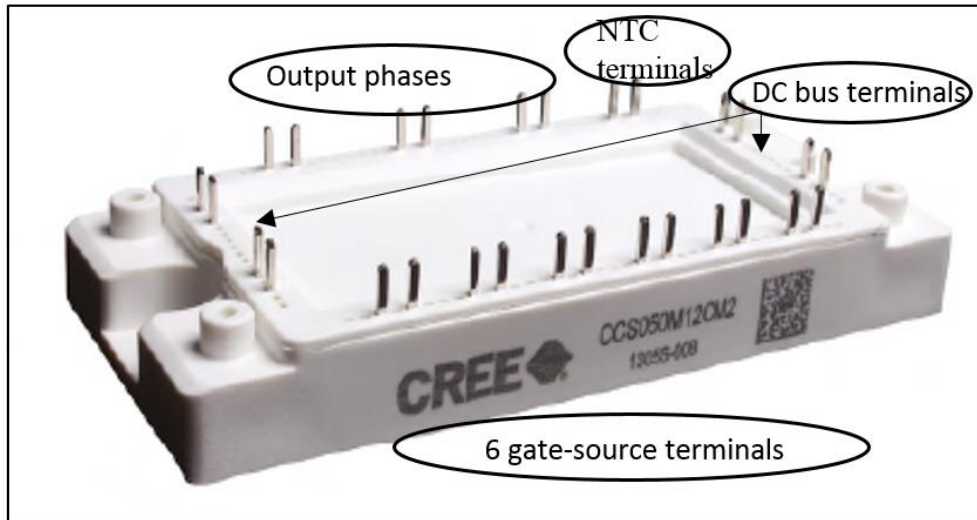
Figure 5.7. All-SiC 6-pack module from Cree (CCS050M12CM2).
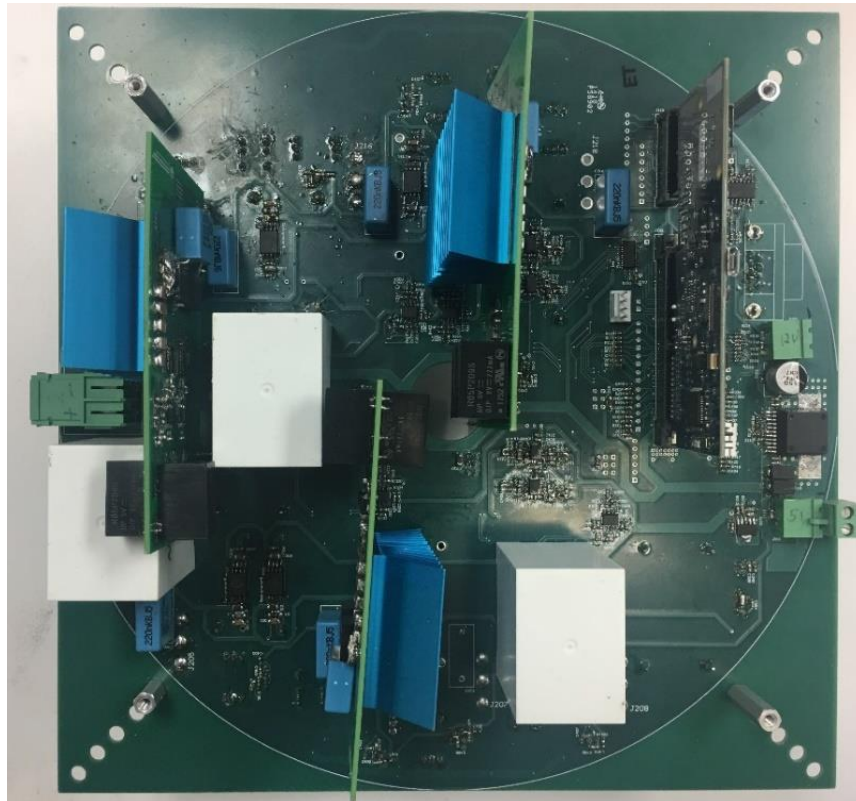
Figure 5.8. Top view of the 6-phase GaN-based motor drive.
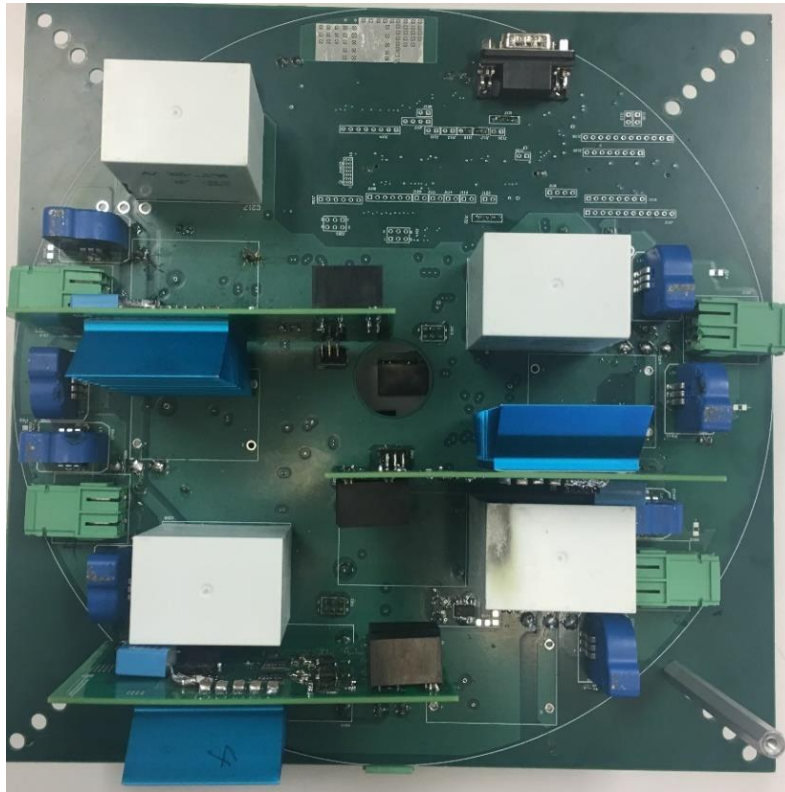
Figure 5.9. Bottom view of the 6-phase GaN-based motor drive.
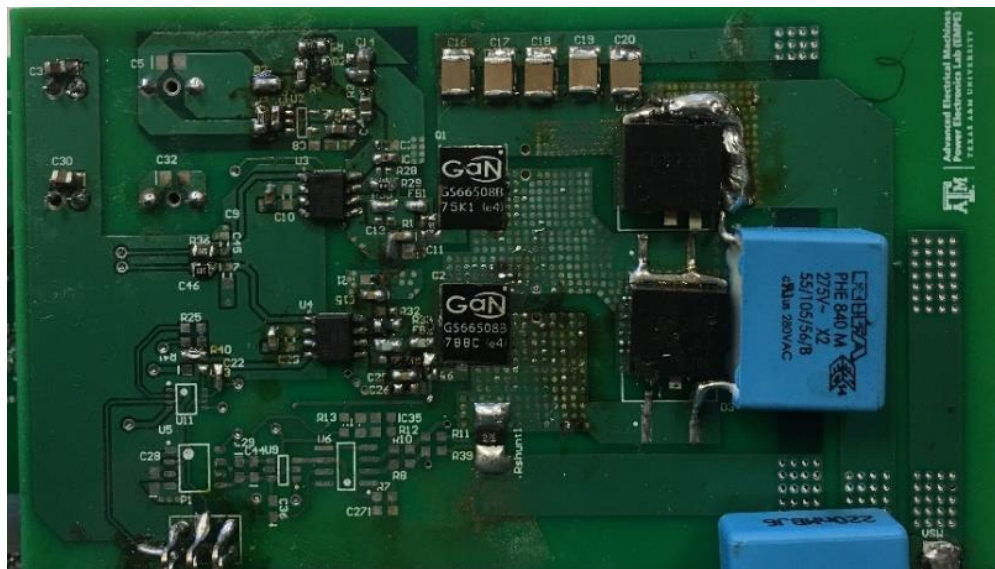
Figure 5.10. Top view of the phase leg unit of the GaN-based motor drive.
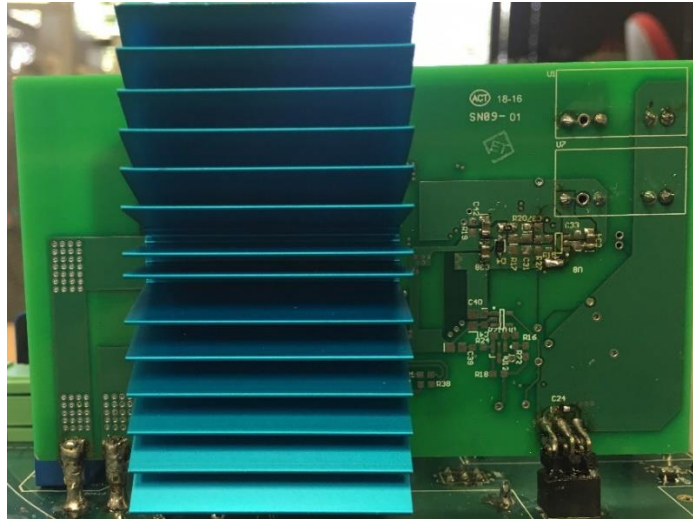
Figure 5.11. Bottom view of the phase leg unit of the GaN-based motor drive.

For the SiC inverter, the dc link consists of several 110 uF metallized polypropylene film capacitors connected in parallel. Each capacitor has a voltage rating of 500 V, an rms current rating of 18.5 A and an equivalent series resistance of 4.4 mΩ. The total dc link capacitance of 770 uF is used. The exact sizing of the dc link capacitance can be found in [109]. This particular design for the dc link has the advantages of a flat dc link capacitor and very low equivalent series resistance and inductance, which helps reduce the commutation loop inductance. In addition to the Panasonic dc link capacitors, a 0.22 µF class X_2 metallized polypropylene film capacitor is placed across the dc link close to each inverter leg for high frequency decoupling.

Figure 5.8 and Figure 5.9 show the GaN-based integrated motor drive (IMD). Table 5.3 shows the part numbers of the main components of the GaN IMD. Table 5.4 shows the most important parameters of the GaN HEMT. The IMD has a compact form

Figure 5.12. Cross section view of GaN package and thermal dissipation path, reprinted from [110].

factor and can be mounted in the end plate region of the motor. The IMD consists of main board and phase-leg boards. The main board has current/voltage sensing circuits, a microcontroller and PCB mounted dc link capacitors. The phase-leg board has GaN devices, a gate drive circuit and overcurrent protection on it. The top and bottom views of the phase leg board are shown in Figure 5.10 and Figure 5.11. The phase-legs can be easily plugged in and out of the main board, which allows easy replacement in case of device failure. The phase-leg board is a 4 layer PCB and the main board has 6 layers.

It uses 650 V, 30 A enhancement mode GaN high electron mobility transistors (HEMT) GS66508B. The proprietary packaging of GaN Systems enables low inductance and low thermal resistance in a small package. The GS66508B is a bottom-side cooled transistor that offers very low junction-to-case thermal resistance for demanding high power applications. It has reverse current capability and zero reverse recovery loss. The bottom side cooling with a heat sink via PCB is the recommended cooling method [110].

61

Table 5.3. Main components of GaN inverter.

Component	Manufacturer Part Number
GaN HEMT	GaN Systems GS66508B
SiC Schottky diode	Rohm SCS220AJTLL
Gate driver	Silicon Labs SI8271AB-IS
DC link film capacitor	KEMET C4AEHBW5400A3LJ
Gate drive isolated supply	Recom Power R05P209S
Current sensor	LEM LTS 25-NP

Table 5.4. GaN transistor datasheet parameters.

Parameter	Value	Units
Rated drain-source voltage, V_{DS}	650	V
Continuous drain current at 25 ℃ case temperature	30	A
Maximum junction temperature	150	℃
On state resistance	50	mΩ
Junction-to-case thermal resistance	0.5	℃/W

The majority of heat, generated in the die, flows down to the thermal pad and then transfers to the PCB. The copper planes on the PCB spread the heat and 0.3 mm diameter thermal vias filled with thermally conductive material provide a low thermal resistance path from the top copper to the bottom side of PCB. A heatsink is attached to the bottom copper plane, as shown in Figure 5.12, via a thermal interface material and dissipates the heat to the ambient environment.

6. EXPERIMENTAL RESULTS

6.1   Details of Experimental Setup

The designed SiC and GaN inverters are tested driving an induction motor. The Figure 6.1 and Figure 6.2 show the experimental setup, which shows the induction motor connected in 6-phase configuration. The squirrel cage induction motor is coupled to a dc generator, which is used to apply the desired load torque. The dc generator is controlled by an ABB DCS800 dc drive. The measurement setup includes a Keysight DSO-X 3024T oscilloscope with 200 MHz bandwidth, Keysight 100 MHz differential voltage probes and Fluke current probes with a 100 kHz bandwidth. A TI TMS320F28379D microcontroller is used to implement the indirect field oriented control of the induction motor.

The motor has wires coming out from all the 36 slots and can be connected as an asymmetrical 6 pole 6-phase or a 6 pole 3-phase motor. The details of the motor are given in Table 6.1. The motor winding layout for the connection of the motor as a 6-phase motor is shown in Figure 6.3 and Figure 6.4. The 3-phase motor is obtained by connecting two phases in series that have 30 degree electrical angle between them i.e. phase A and D, phase B and E, and phase C and F are connected in series. The motor is connected in star in both 3-phase and 6-phase configurations for testing. The SiC inverter is tested with both the 3-phase and 6-phase motor configurations. The GaN inverter is tested with the 3-phase motor configuration.
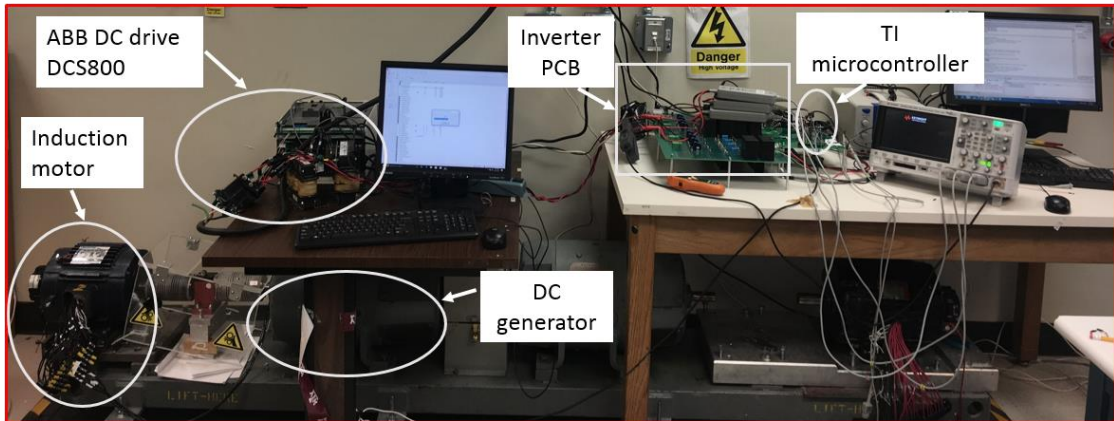
Figure 6.1. Experimental setup for testing of motor drives.
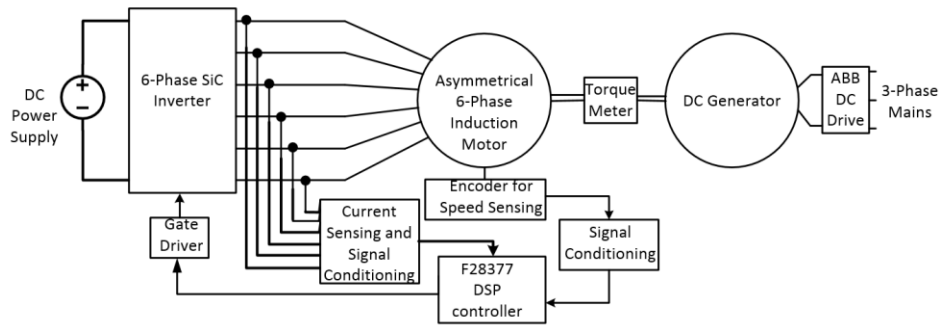
Figure 6.2. Layout of experimental setup for testing of motor drives.
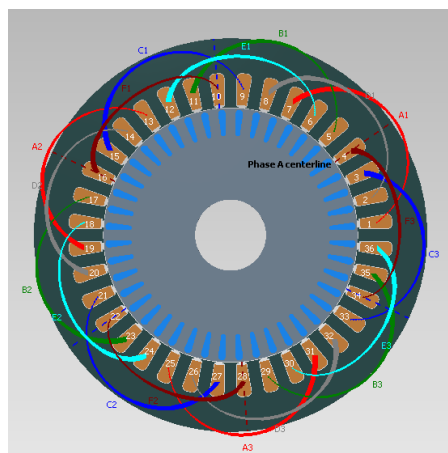
Figure 6.3. Winding layout for the 6-phase motor.

64

Table 6.1 Motor details.

Type	Quantity	Value
NAMEPLATE	Rated Power	3 HP
	Rated Speed	1200 RPM
	Rated Voltage	460 V
	Poles	6
STATOR	Number of Slot	36
	Number of Parallel Paths	1
	Turns per Slot	44
	Winding layers	1
	Thermocouples	3, one in each phase a, b and c
	Magnet wire used	GPMR 200 (Heavy build, 200 ℃)
	Search coils	Back Iron Flux, Tooth Flux, Coil A1 flux, Coil D1 Flux
	Phase Separator	VAR-H Glass Cloth Class H (180 ℃)
	Slot insulation	DMD (Dacron Mylar Dacron), Class F (155 ℃), DM 5-5-5
EQUIVALENT CIRCUIT (3-phase motor)	Number of Bars	36
	L_m	0.132 H
	L_{ls}	10.43 mH
	R_s	3.18 Ohm
	L_{lr}	10.43 mH
EQUIVALENT CIRCUIT (6-phase motor)	R_r	1.55 Ohm
	L_m	0.0729 H
	Ll_s	6.46 mH
	R_s	2.2 Ohm
	L_{lr}	6.46 mH
	R_r	3.05 Ohm

```
Layout of phase A          Coil #  |  Go  |  Return
                           1       |  1   |  7
                           2       |  13  |  19
                           3       |  25  |  31

Layout of phase B          Coil #  |  Go  |  Return
                           1       |  5   |  11
                           2       |  17  |  23
                           3       |  29  |  35

Layout of phase C          Coil #  |  Go  |  Return
                           1       |  9   |  15
                           2       |  21  |  27
                           3       |  33  |  3

Layout of phase D          Coil #  |  Go  |  Return
                           1       |  2   |  8
                           2       |  14  |  20
                           3       |  26  |  32

Layout of phase E          Coil #  |  Go  |  Return
                           1       |  6   |  12
                           2       |  18  |  24
                           3       |  30  |  36

Layout of phase F          Coil #  |  Go  |  Return
                           1       |  10  |  16
                           2       |  22  |  28
                           3       |  34  |  4
```

Figure 6.4. Winding layout for the 6-phase motor with coil in and out slots.

6.2   Digital Implementation of the Motor Control Loop

A block diagram of the indirect field oriented control (IFOC) of the 6-phase asymmetrical induction motor (IM), which is implemented in a F28377 digital signal processor (DSP), is shown in Figure 6.5. The control block diagram of the 3-phase IM is well known and is not discussed in this dissertation. Speed is sensed using an encoder. The d-axis current command is fixed and q-axis current command is generated by the speed control loop. The x-axis and y-axis current commands are set to zero because these currents just cause losses. The zero sequence voltage references are set to zero. The control algorithm is implemented using TI's IQmath libraries. The switching signals are generated using space vector PWM.

66

Figure 6.5. Block diagram of the indirect field oriented control of 6-phase asymmetrical induction motor implemented in F28377 DSP.

6.3 Experimental Results Demonstrating Performance of SiC-based Induction Motor Drive

The design and performance of the SiC inverter is validated by driving the induction motor connected in the 3-phase and 6-phase configurations. The switching waveforms of the SiC MOSFETs are shown in Figure 6.6 and Figure 6.7. It can be seen that the rise time of the drain-source voltage is around 24 ns and the fall time is 22 ns, and the overshoot in the drain-source voltage is 10% for a dc link voltage of 200 V.
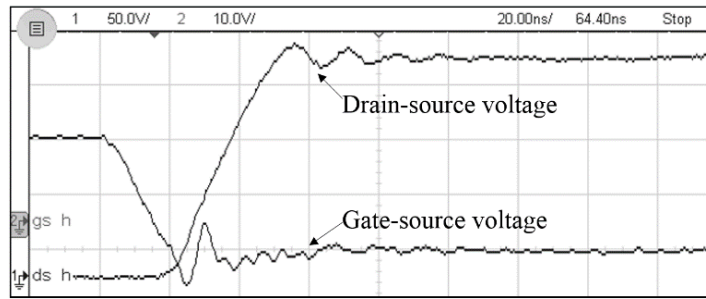
Figure 6.6. Drain-source and gate-source voltage of SiC MOSFET showing rise time in the SiC-based induction motor drive.
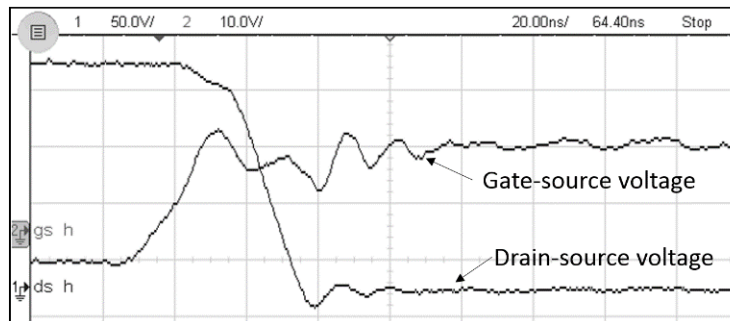

Figure 6.7. Drain-source and gate-source voltage of SiC MOSFET showing fall time in the SiC-based induction motor drive.
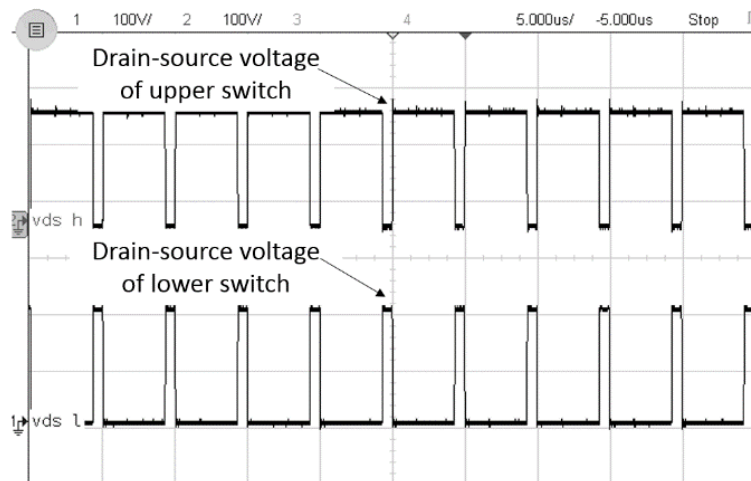
Figure 6.8. Drain-source voltage of both switches of a phase leg in the SiC-based induction motor drive.

68
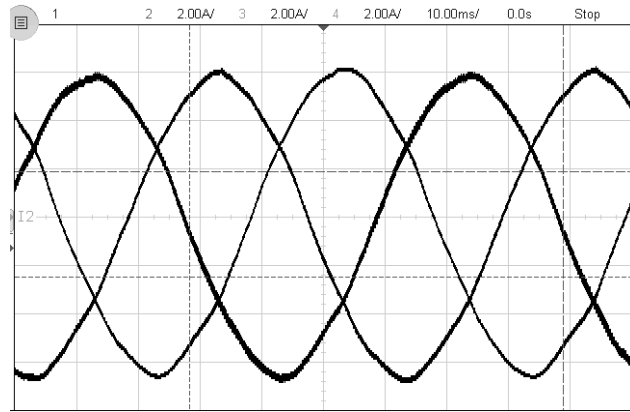
Figure 6.9. Stator currents of the motor in SiC-based 3-phase induction motor drive.

It can be seen that in Figure 6.6, the spike in the gate-source voltage during off-state due to Miller effect is well below the threshold voltage of 2.1 V for SiC MOSFET. Also, the gate-source voltage overshoot or undershoot does not exceed the dynamic rating (-8/+19 V) of the gate-source terminal. The results shown in Figure 6.8 verify the operation of the inverter at 200 kHz to demonstrate the high switching frequency capability of the designed SiC inverter. The stator currents of the SiC-based 3-phase motor drive are shown in Figure 6.9 with motor running at 317 r/min. The motor is able to run in closed loop in steady state, without abnormal high-frequency current ripple, which further confirms the effectiveness of the inverter design.

Figures 6.10 to 6.13 show the rise and fall times of both the switches in a phase leg recorded at the positive peak of the current waveform at different dc link voltages and line currents. Figures 6.10 to 6.11 and Figures 6.12 to 6.13 show the rise and fall times for two different line currents at dc link voltages of 35 V and 150 V respectively. It can be seen that the turn-off speed of a switch depends on the magnitude of the current being commutated and the dc link voltage. The switch turns off faster at higher values of current

for a given dc link voltage, as shown in Figure 6.10 and Figure 6.11 for 35 V dc link voltage, and in Figure 6.12 and Figure 6.13 for 150 V dc link voltage, for two different values of currents. The turn-off process of a switch will take longer for a higher dc link voltage at a given current as shown in Figure 6.12 and Figure 6.13 for 2.1 A current at two different dc link voltages of 35 V and 150 V. The inverter is operated with a dead time of 100 ns after recording the switching times at different operating conditions. Figure 6.14 shows the switching times at a 200 V dc link voltage and a 4.5 A rms current.
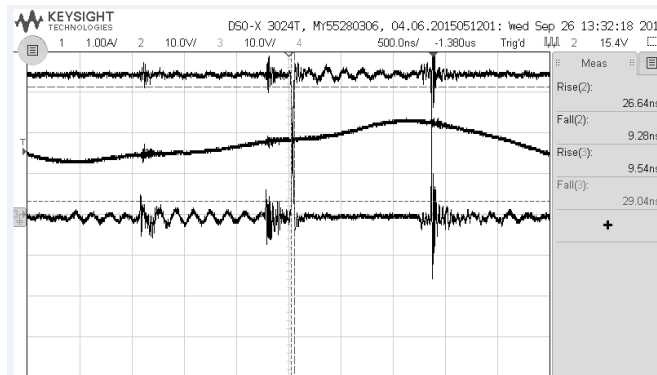
Figure 6.10. Rise and fall times of both the switches of a phase leg in the SiC-based 3-phase induction motor drive at 35 V, 1.31 A rms current (motor speed of 86 rpm).
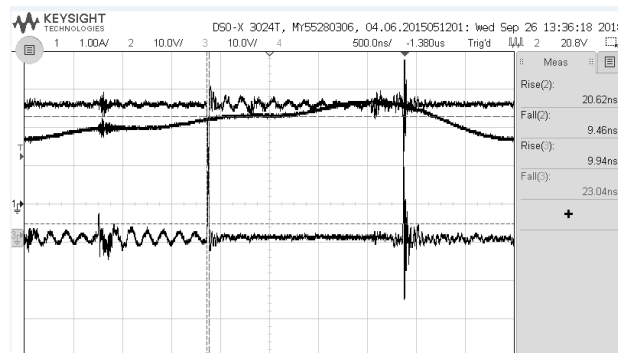
Figure 6.11. Rise and fall times of both the switches of a phase leg in the SiC-based 3-phase induction motor drive at 35 V, 2.1 A rms current (motor speed of 56 rpm).
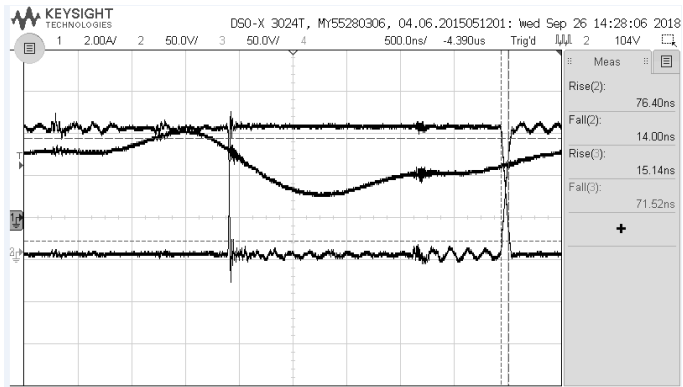
Figure 6.12. Rise and fall times of both the switches of a phase leg in the SiC-based 3-phase induction motor drive at 150 V, 2.1 A rms current (motor speed of 334 rpm).
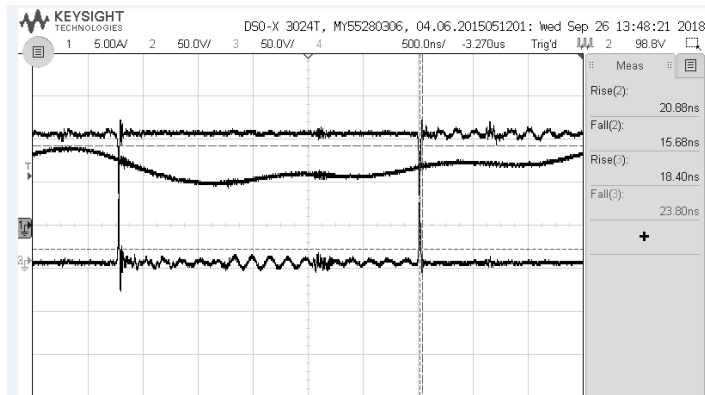
Figure 6.13. Rise and fall times of both the switches of a phase leg in the SiC-based 3-phase induction motor drive at 150 V, 5.31 A rms current (motor speed of 175 rpm).
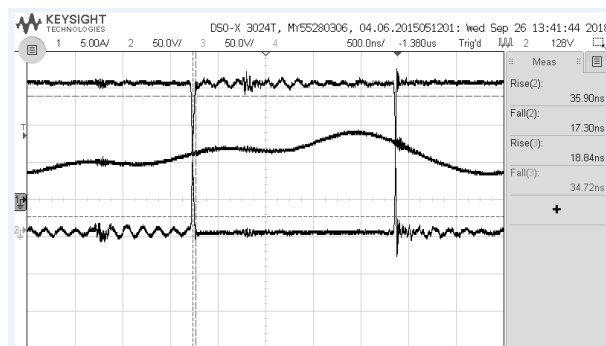
Figure 6.14. Rise and fall times of both the switches of a phase leg in the SiC-based 3-phase induction motor drive at 200 V, 4.5 A rms current (motor speed of 274 rpm).

Figure 6.15. Torque response of SiC-based 3-phase induction motor drive showing output of torque meter and 3-phase currents (torque reference changed from 5 Nm to 10 Nm at 290 rpm).
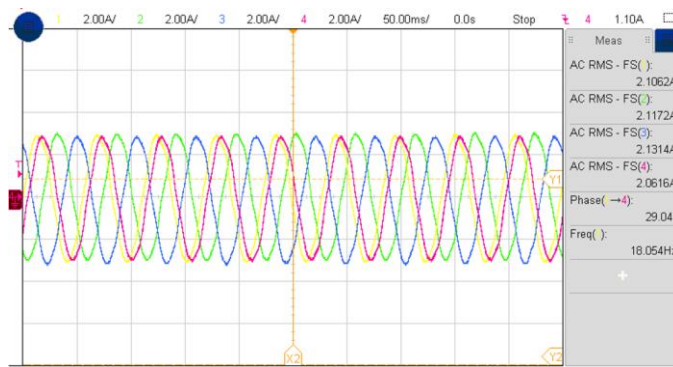
Figure 6.16. Stator currents of the SiC-based 6-phase asymmetrical induction motor drive running at 352 rpm (All 3 currents of first 3 phase set shown on first 3 channels and first current of second 3 phase set shown on channel 4: 30 degree phase shift shown between channel 1 and 4).

Figure 6.15 shows the response of 3-phase IM switching when the torque is ramped from 5 Nm to 10 Nm. Figure 6.16 shows the motor currents of the SiC-based 6-phase IM drive and Figure 6.17 shows the response when the speed is ramped from 75 rpm to 150 rpm.

6.3.1 *Advantage of WBG Devices for Multiphase Motor Drives*

For studying the effect of the dead time of inverter on the currents in the x-y subspace of multiphase motor drives, the SiC inverter is operated at a switching frequency of 20 kHz that is typical for Si IGBT-based drives. The currents in x-y or zero sequence subspaces are not controlled. Generally, a dead time of 2 us or higher is used for Si IGBT-based drives. Figure 6.18 shows the current waveforms of an asymmetrical 6-phase motor for different values of dead time of the inverter. It can be seen that the current waveform has significant distortion for a dead time of 2 us or higher. The distortion is due to harmonic currents of the order of 5, 7 and higher, which are caused due to effect of dead time. For a dead time of 500 ns or lower, that are possible only with WBG device-based drives, the current waveform is very close to sinusoidal. Thus, WBG device-based drives do not require control of currents in x-y subspace if there is no asymmetry in the converter or motor.

6.4 **Experimental Results Demonstrating the Performance of GaN-based Induction Motor Drive**

Figure 6.19 shows the switching waveform of a GaN switch in a 3-phase IM drive, which exhibits excellent switching performance. The motor currents are shown in Figure 6.20. Figure 6.21 shows the torque response when the torque is ramped from 3.75 Nm to 7.5 Nm and then back to 3.75 Nm. Speed control response is shown in Figure 6.22 when the speed is ramped from 75 rpm to 150 rpm.
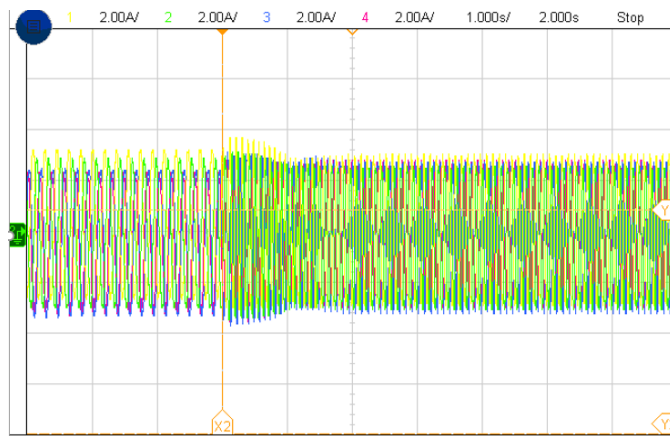
Figure 6.17. Speed control response of the SiC-based 6-phase asymmetrical induction motor drive (Speed reference change from 75 rpm to 150 rpm at 6.75 Nm torque, all 3 currents of first 3 phase set shown on first 3 channels and first current of second 3 phase set shown on channel 4).
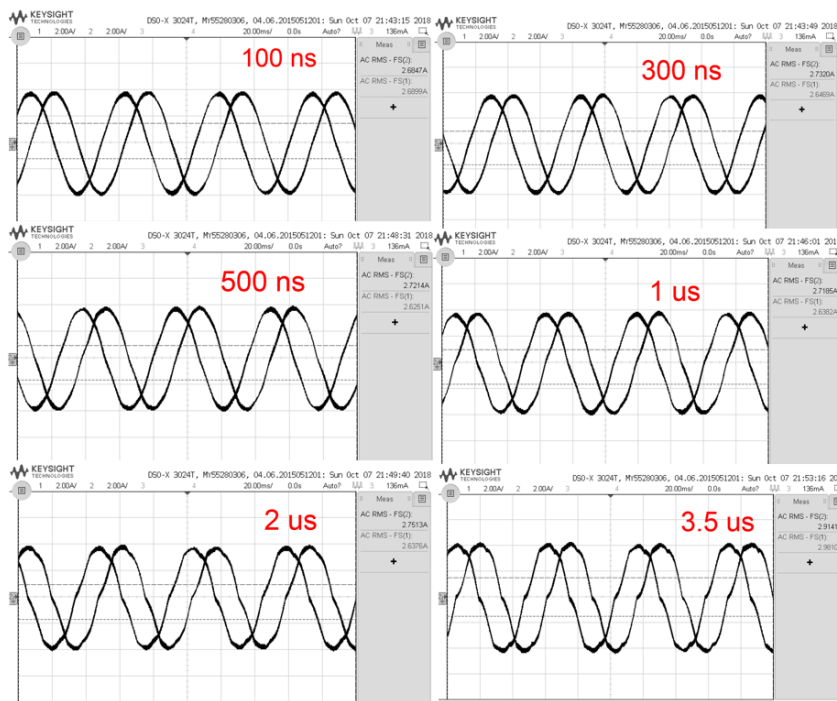
Figure 6.18. Current waveforms of an asymmetrical 6-phase motor for different values of dead time of the inverter (Motor running at 280 rpm, 2.7 A rms current, one from each 3-phase set is shown).

74
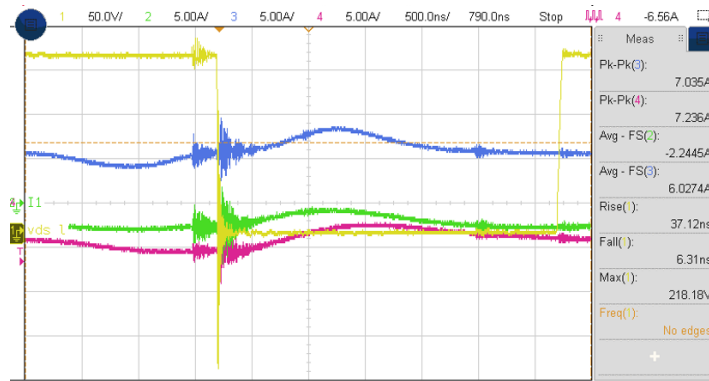
Figure 6.19. Switching waveform of the GaN switch in a phase leg captured the peak of the current in the GaN-based 3-phase induction motor (rise time=37.12 ns and fall time=6.31 ns at 200 V dc bus voltage 4.6 A rms current).
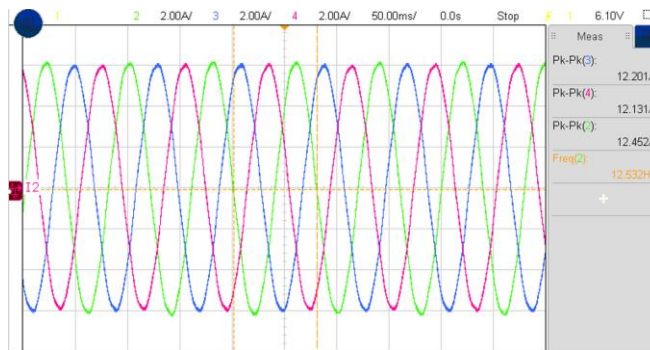
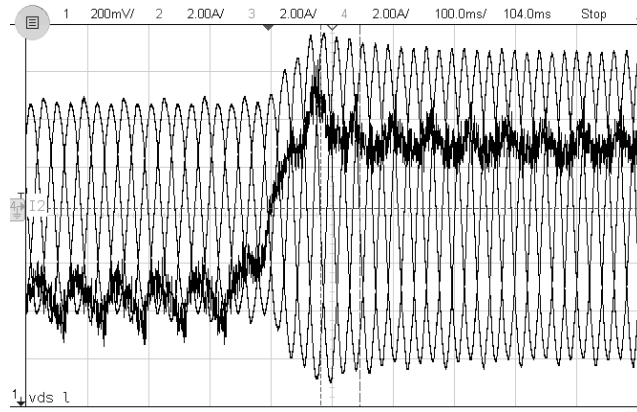Figure 6.20. Stator currents of the GaN-based 3-phase induction motor drive.
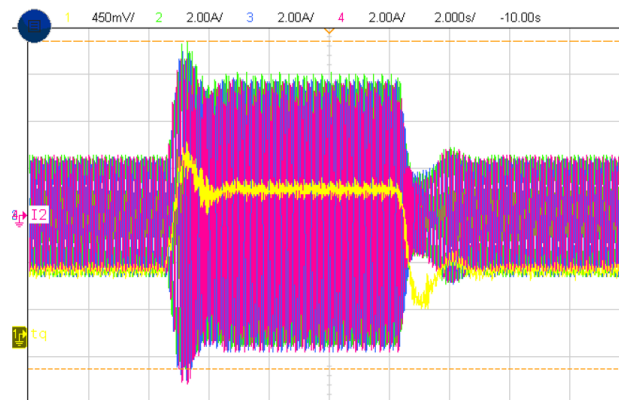
Figure 6.21. Torque response of the GaN-based 3-phase induction motor drive showing output of torque meter and 3-phase currents (Torque reference sequence at 150 rpm: 3.75 Nm->7.5 Nm ->3.75 Nm).

75
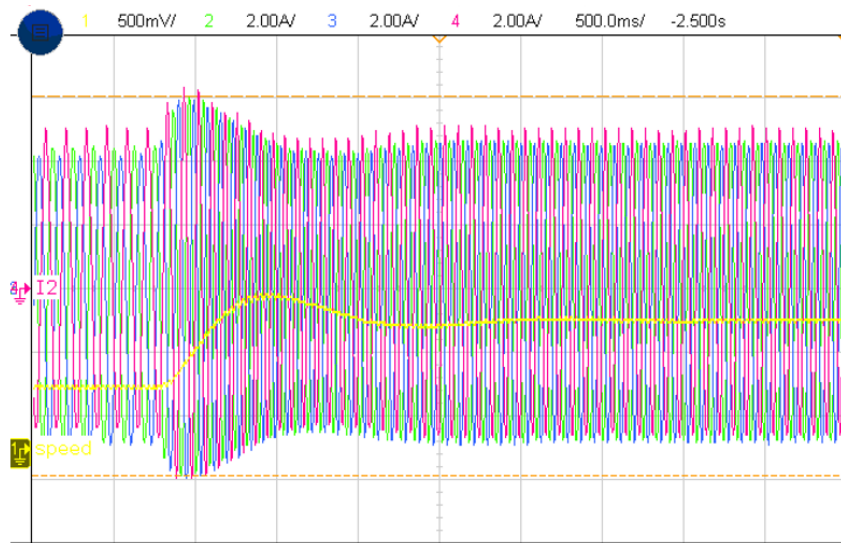
Figure 6.22. Speed control response of the GaN-based 3-phase induction motor drive showing a signal proportional to speed and 3-phase currents (Speed reference change from 75 rpm to 150 rpm at 6.75 Nm torque).
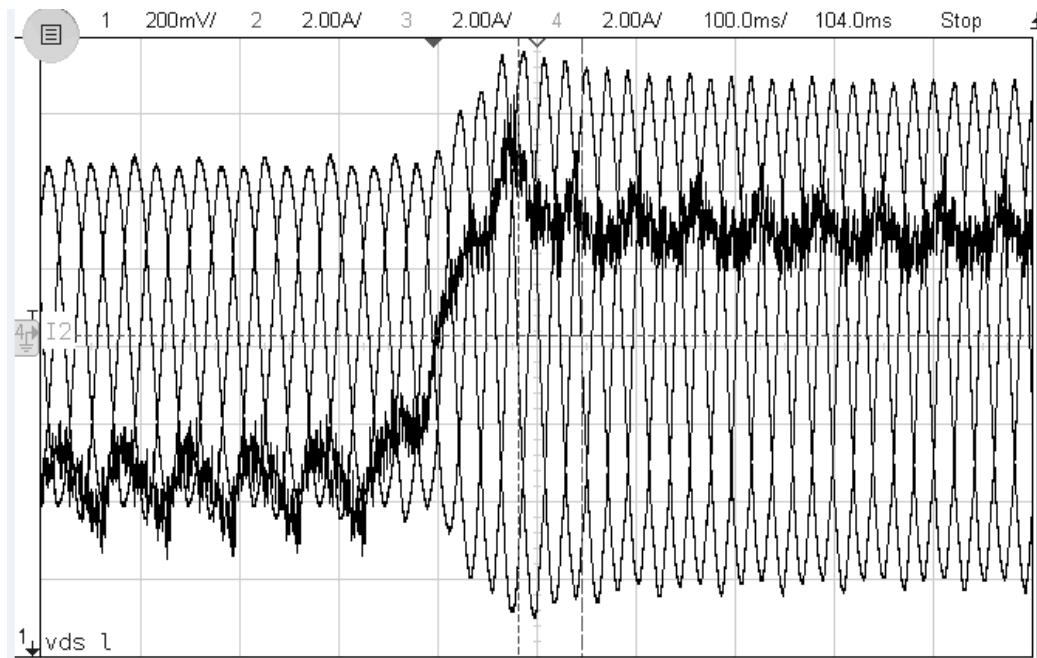
Figure 6.23. Torque increase from 3 Nm to 6 Nm with twice the current during 3-phase operation.

6.5   Experimental Validation of the Higher Short-term Torque Capability of the Invention

The increase in torque and the time rating of the induction motor with twice the rated current are presented.

6.5.1   *Torque of the Asymmetrical 6-Phase Motor in 3-Phase Configuration With Twice the Rated Current*

Figure 6.23 shows the 3-phase currents and the torque of the motor in 3-phase configuration; the dark line shows the torque. The torque increases from 3 Nm to 6 Nm when twice the torque producing component of current is forced.

6.5.2   *Temperature Rise of the Induction Motor With Twice the Rated Current*

The induction motor is totally enclosed type with power rating and current rating of 3 HP and 4.4 A respectively. The GPMR magnet wire of the motor is rated at 200 °C. The phase separator insulation is class H insulation, which is rated at 180 °C. The slot liner is class F insulation, which is rated at 155 °C. The winding temperature is measured using a K-type thermocouple that is placed in the end winding, which is considered the hottest part of the winding. For finding the time rating for twice the rated current, the motor is run at rated current for 4 hours till a steady temperature of 133 °C is reached. After that, the motor current is rapidly increased to 8.8 A that is twice the rated current. The winding temperature increased from 134 °C to 151 °C in 17 s as shown in Figure 6.24. The lowest temperature class insulation used in this motor is slot liner, which is rated for 155 °C. The hot spot temperature is generally 10 °C higher than the average temperature in a winding. Therefore, the winding temperature must not exceed 145 °C that

is reached in 12 s. Therefore, we can conclude that the time rating of the motor for twice the rated current is 12 s.

Time (s)	T (°C)
1	134
2	135
3	136
4	137
5	138
6	139
7	140
8	141
9	142
10	143
11	144
12	145
13	146
14	147
15	148
16	149
17	150
18	151
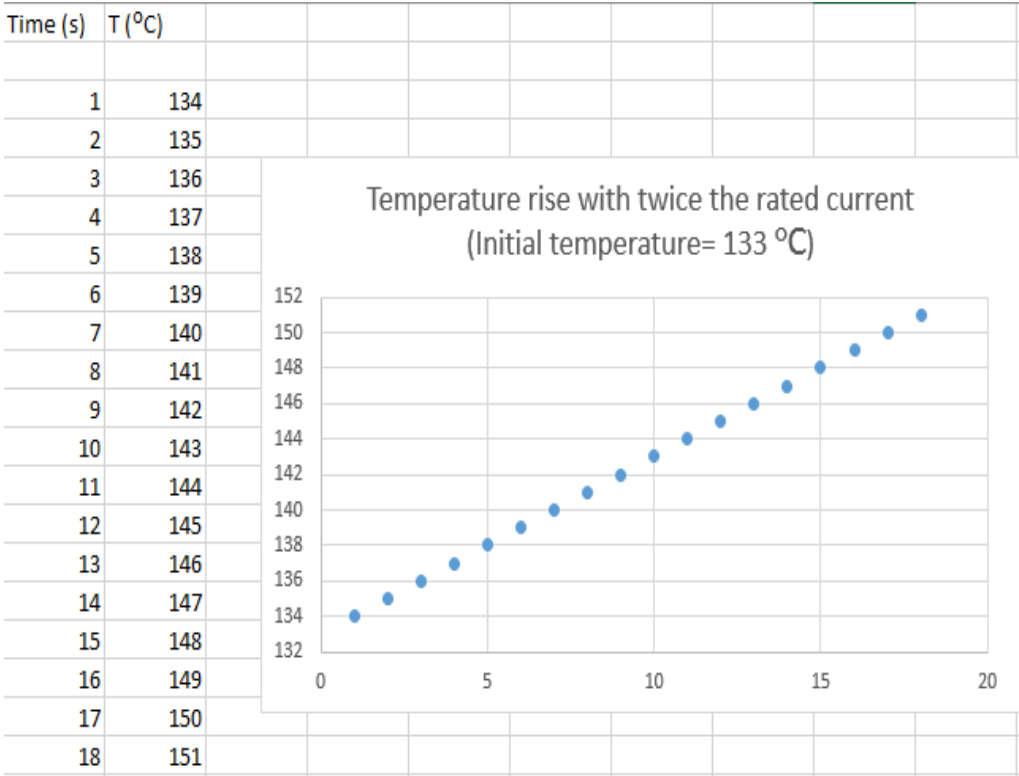
Figure 6.24. Temperature rise of the induction motor with twice the rated current.

7. CONCLUSION AND FUTURE WORK

WBG devices enable the next generation of efficient and lightweight motor drives for use in various applications. WBG devices are an enabling technology for many motor drive applications and especially beneficial for low-inductance motors, high-speed motors and high-temperature applications. However, to achieve the maximum benefits from using WBG devices, the converter must be designed with appropriate gate drivers that can switch quickly with minimal overshoot and losses, with minimal parasitic inductance in the commutation loop, and with fast short-circuit protection for the WBG switches.

The trade-off between high switching frequency and other issues such as high *dv/dt* and electromagnetic interference needs to be considered. The challenges in designing WBG device-based converters are discussed and design considerations are illustrated with developed SiC and GaN-based motor drives. The performances of the developed motor drives are demonstrated with experimental results, which proves the effectiveness of the designs. The problem of insulation damage due to high dv/dt in WBG device-based inverters is discussed in detail and the insulation design considerations are presented. The system level benefits and energy savings due to the high efficiency obtained using SiC devices can offset their high cost. WBG devices are key technologies for vehicle electrification and can be expected to make EVs more efficient and economical in the near future.

The invention of a system reconfiguration and control technique for a multiphase motor drive to obtain up to 93% higher torque for applications requiring high transient

torque is presented. This invention can exploit the peak rating of the motor by incorporating the thermal time ratings of the motor in control strategies. The feedback of the motor temperature will help in getting maximum performance from this invention.

The WBG devices have multiple advantages for multiphase motor drives. The 5th and 7th harmonics in the voltage due to dead time in an inverter can be reduced significantly with WBG devices. This will result in a reduction in currents in the xy subspace, which cause heating in windings. The high bandwidth current control, enabled by the high switching frequency capability of WBG devices, in higher subspaces of multiphase motor drives makes it possible to significantly reduce the currents in those subspaces. These benefits of WBG devices for multiphase motor drives can be quantified and more benefits can be explored for different multiphase motors.

REFERENCES

[1]   J. Millán, P. Godignon, X. Perpiñà, A. Pérez-Tomás and J. Rebollo, "A Survey of Wide Bandgap Power Semiconductor Devices," *IEEE Trans. Power Electron.*, vol. 29, no. 5, pp. 2155-2163, May 2014.

[2]   J. W. Palmour *et alia*, "Silicon carbide power MOSFETs: Breakthrough performance from 900 V up to 15 kV," in *proc. 26th Int. Symp. on Power Semicond. Devices & IC's (ISPSD)*, Waikoloa, HI, Jun. 2014, pp. 79-82.

[3]   T. P. Chow, I. Omura, M. Higashiwaki, H. Kawarada and V. Pala, "Smart Power Devices and ICs Using GaAs and Wide and Extreme Bandgap Semiconductors," *IEEE Trans. Electron. Devices*, vol. 64, no. 3, pp. 856-873, Mar. 2017.

[4]   A. Bindra, "Wide-Bandgap-Based Power Devices: Reshaping the power electronics landscape," *IEEE Power Electron. Mag.*, vol. 2, no. 1, pp. 42-47, Mar. 2015.

[5]   A. Agarwal, L. Marlino, R. Ivester and M. Johnson, "Wide Bandgap power devices and applications; the U.S. initiative," *in proc. 46th European Solid-State Device Research Conf. (ESSDERC)*, Lausanne, Sep. 2016, pp. 206-209. K.;

[6]   R. Eden, Principal analyst, Power semiconductors at IHS Markit "Market for GaN and SiC power semiconductors to top $10 billion in 2027" https://technology.ihs.com/602187/market-for-gan-and-sic-power semiconductors-to-top-10-billion-in-2027.

[7]   P. Roussel, "SiC market and industry update," presented at the Int. SiC Power Electron. Appl. Workshop, Kista, Sweden, 2011.

[8]   A. Lidow, D. Reusch, J. Wilhelm Strydom, and M. de Rooij, GaN Transistors for Efficient Power Conversion, 2nd ed., Chichester, United Kingdom, John Wiley & Sons Ltd., Jun. 26, 2014, pp. 39-54.

[9]   A. Mohamed, F. EL-Refaie, R. Dean King, "Low-inductance, high-efficiency induction machine and method of making same," US Patent 20120126741 A1, May 24, 2012.

[10]   H. Mirzaee, S. Bhattacharya, S. H. Ryu and A. Agarwal, "Design comparison of 6.5 kV Si-IGBT, 6.5kV SiC JBS diode, and 10 kV SiC MOSFETs in megawatt converters for shipboard power system," in *proc. Elect. Ship Technol. Symp.*, Alexandria, VA, Apr. 2011, pp. 248-253

[11]   H. Mirzaee, S. Bhattacharya, S. H. Ryu and A. Agarwal, "Design comparison of 6.5 kV Si-IGBT, 6.5kV SiC JBS diode, and 10 kV SiC MOSFETs in megawatt converters for shipboard power system," in *Proc. Elect. Ship Technol. Symp.*, Alexandria, VA, Apr. 2011, pp. 248-253.

[12]   D. Gerada, A. Mebarki, N. L. Brown, C. Gerada, A. Cavagnino and A. Boglietti, "High-Speed Electrical Machines: Technologies, Trends, and Developments," *IEEE Trans. Ind. Electron.*, vol. 61, no. 6, pp. 2946-2959, Jun. 2014.

[13]   J. Hornberger, A. B. Lostetter, K. J. Olejniczak, T. McNutt, S. M. Lal and A. Mantooth, "Silicon-carbide (SiC) semiconductor power electronics for extreme high-temperature environments," in *proc. 2004 IEEE Aerospace Conf. (IEEE Cat. No.04TH8720)*, Big Sky, MT, Mar. 2004, pp. 2538-2555 Vol.4.

[14]   B. Wrzecionko, D. Bortis and J. W. Kolar, "A 120 °C Ambient Temperature Forced Air-Cooled Normally-off SiC JFET Automotive Inverter System," *IEEE Trans. Power Electron.*, vol. 29, no. 5, pp. 2345-2358, May 2014.

[15]   M. A. Masrur, "Toward Ground Vehicle Electrification in the U.S. Army: An Overview of Recent Activities," *IEEE Electrific. Mag.*, vol. 4, no. 1, pp. 33-45, Mar. 2016.

[16]   B. Bilgin et al., "Making the Case for Electrified Transportation," *IEEE Trans. Transportation Electrific.*, vol. 1, no. 1, pp. 4-17, Jun. 2015.

[17]   "Variable speed drives by WEG electric corp." available at http://ecatalog.weg.net/files/wegnet/WEG-cfw11-system-drive-50019076-brochure-english.pdf

[18]   Zero to 60 Times https://www.zeroto60times.com/

[19]   V. T. Buyukdegirmenci and P. T. Krein, "Induction Machine Characterization for Short-Term or Momentary Stall Torque," *IEEE Trans. Ind. Appl.*, vol. 51, no. 3, pp. 2237-2245, May-Jun. 2015.

[20]   E. Levi, R. Bojoi, F. Profumo, H. A. Toliyat and S. Williamson, "Multiphase induction motor drives - a technology status review," *IET Electric Power Appl.*, vol. 1, no. 4, pp. 489-516, Jul. 2007.

[21]   M. Su, C. Chen, S. Sharma and J. Kikuchi, "Performance and cost considerations for SiC-based HEV traction inverter systems," *in proc. 3rd Workshop on Wide Bandgap Power Devices and Appl. (WiPDA)* ,Blacksburg, VA, Nov. 2015, pp. 347-350.

[22]   J. O. Krah and J. Holtz, "High-performance current regulation and efficient PWM implementation for low-inductance servo motors," *IEEE Trans. Ind. Appl.*, vol. 35, no. 5, pp. 1039-1049, Sep./Oct. 1999.

[23]   Gui-Jia Su and D. J. Adams, "Multilevel dc link inverter for brushless permanent magnet motors with very low inductance," in *proc. 2001 IEEE Ind. Appl. Conf. 36th IAS Annual Meeting (Cat. No.01CH37248)*, Chicago, IL, USA, 2001, pp. 829-834 vol.2.

[24]   Gui-Jia Su and D. J. Adams, "Multilevel dc link inverter for brushless permanent magnet motors with very low inductance," in *proc. 2001 IEEE Ind. Appl. Conf. 36th IAS Annual Meeting (Cat. No.01CH37248)*, Chicago, IL, USA, 2001, pp. 829-834 vol.2.

[25]   M. Novák, J. Novák and O. Sivkov, "An SiC inverter for high speed permanent magnet synchronous machines," in *proc. IECON - 41st Annu. Conf. of the IEEE Ind. Electron. Soc.*, Yokohama, 2015, pp. 002397-002402.

[26]   Y. Li, D. Han, N. Altintas and B. Sarlioglu, "Design of high-speed toroidal winding surface PM machine with SiC-based inverters," *in proc. XXII Int. Conf. on Elect. Mach. (ICEM)*, Lausanne, 2016, pp. 1559-1565.

[27]   D. Gerada, A. Mebarki, N. L. Brown, C. Gerada, A. Cavagnino and A. Boglietti, "High-Speed Electrical Machines: Technologies, Trends, and Developments," *IEEE Trans. Ind. Electron.*, vol. 61, no. 6, pp. 2946-2959, Jun. 2014.

[28]   "DE-FOA-0001208: Next generation electric machines: megawatt class motors," Department of Energy (DOE), Office of Energy Efficiency and Renewable Energy (EERE), [Online]. Available: https://energy.gov/eere/amo/next-generation-electric-machines.

[29]   B. Passmore, C. O'Neal, Wolfspeed "High-Voltage SiC Power Modules for 10-25 kV Applications" [Online]. Available: http://www.powermag.com/pdf/feature_pdf/1461163294_Woifspeed_Feature.pdf

[30]   R. Abebe et al., "Integrated motor drives: state of the art and future trends," IET Elect. Power Appl., vol. 10, no. 8, pp. 757-771, Sep. 2016.

[31]   "US Department of energy (DOE) ,Office of energy efficiency and renewable energy (EERE), Vehicle Technology Office (VTO): Overview of the DOE Advanced Power Electronics and Electric Motor (APEEM) R&D Program," [Online] Available: http://energy.gov/sites/prod/files/2014/09/f18/fy_2014_vto_amr_apeem_overview-final_version.pdf   on Nov. 30, 2016.

[32] "About the SiC MOSFET Modules in Tesla Model 3" [Online]. Available:"https://www.pntpower.com/tesla-model-3-powered-by-st-microelectronics-sic-mosfets/

[33] Y. Zhao and T. A. Lipo, "Space vector PWM control of dual three-phase induction machine using vector space decomposition," *IEEE Trans. Ind. Appl.*, vol. 31, no. 5, pp. 1100-1109, Sep.-Oct. 1995.

[34] H. S. Che et al. "Current Control Methods for an Asymmetrical Six-Phase Induction Motor Drive," *IEEE Trans. Power Electron.*, vol. 29, no. 1, pp. 407-417, Jan. 2014.

[35] D. G. Dorrell, A. M. Knight, L. Evans and M. Popescu, "Analysis and Design Techniques Applied to Hybrid Vehicle Drive Machines—Assessment of Alternative IPM and Induction Motor Topologies," *IEEE Trans. Ind. Electron.*, vol. 59, no. 10, pp. 3690-3699, Oct. 2012.

[36] M. Kato, K. Orikawa, J. i. Itoh and N. Saitoh, "Fast starting method using both inverter and delta-star starter for weaving machine drive systems," in *proc. 2013 1st Int. Future Energy Electron. Conf. (IFEEC)*, Tainan, 2013, pp. 211-216.

[37] Speed hack: Attaining supercar acceleration via software (Farday Future-FutureSight) Available at: https://www.ff.com/en/futuresight/0-60-acceleration-test/.

[38] B. S. Umesh and K. Sivakumar, "Multilevel Inverter Scheme for Performance Improvement of Pole-Phase-Modulated Multiphase Induction Motor Drive," *IEEE Trans. Ind. Electron.*, vol. 63, no. 4, pp. 2036-2043, Apr. 2016.

[39] J. Lemmens, J. Driesen and P. Vanassche, "Dynamic DC-link voltage adaptation for thermal management of traction drives," in Proc. *2013 IEEE Energy Convers. Congr. Expo.*, Denver, CO, 2013, pp. 180-187.

[40] N. Sakib, M. Manjrekar and A. Ebong, "An overview of advances in high reliability gate driving mechanisms for SiC MOSFETs," in *proc. IEEE 5th Workshop on Wide Bandgap Power Devices and Applicat. (WiPDA)*, Albuquerque, NM, USA, 2017, pp. 291-294.

[41] A. P. Camacho, V. Sala, H. Ghorbani and J. L. R. Martinez, "A Novel Active Gate Driver for Improving SiC MOSFET Switching Trajectory," *IEEE Trans. Ind. Electron.*, vol. 64, no. 11, pp. 9032-9042, Nov. 2017.

[42] D. Peftitsis and J. Rabkowski, "Gate and Base Drivers for Silicon Carbide Power Transistors: An Overview," *IEEE Trans. Power Electron.*, vol. 31, no. 10, pp. 7194-7213, Oct. 2016.

[43]   S. Yin, K. J. Tseng, C. F. Tong and R. Simanjorang, "Design of high-speed gate driver to reduce switching loss and mitigate parasitic effects for SiC MOSFET," *IET Power Electron.*, vol. 10, no. 10, pp. 1183-1189, 8 18 2017.

[44]   C. DiMarino, J. Wang, R. Burgos and D. Boroyevich, "A high-power-density, high-speed gate driver for a 10 kV SiC MOSFET module," in *proc. IEEE Electric Ship Technol. Symp. (ESTS)*, Arlington, VA, 2017, pp. 629-634.

[45]   R. Gao, L. Yang, W. Yu and I. Husain, "Gate driver design for a high power density EV/HEV traction drive using silicon carbide MOSFET six-pack power modules," in *proc. IEEE Energy Convers. Congr. and Expo. (ECCE)*, Cincinnati, OH, 2017, pp. 2546-2551.

[46]   D. P. Sadik, K. Kostov, J. Colmenares, F. Giezendanner, P. Ranstad and H. P. Nee, "Analysis of Parasitic Elements of SiC Power Modules With Special Emphasis on Reliability Issues," *IEEE J. Emerg. and Sel. Topics in Power Electron.*, vol. 4, no. 3, pp. 988-995, Sep. 2016.

[47]   T. Liu, R. Ning, T. T. Y. Wong and Z. J. Shen, "Modeling and Analysis of SiC MOSFET Switching Oscillations," I*EEE J. Emerging and Sel. Topics in Power Electron.*, vol. 4, no. 3, pp. 747-756, Sep. 2016.

[48]   M. Ando and K. Wada, "Design of Acceptable Stray Inductance Based on Scaling Method for Power Electronics Circuits," *IEEE J. Emerging and Sel. Topics in Power Electron.*, vol. 5, no. 1, pp. 568-575, Mar. 2017.

[49]   A. Lemmon, M. Mazzola, J. Gafford and C. Parker, "Instability in Half-Bridge Circuits Switched With Wide Band-Gap Transistors," *IEEE Trans. Power Electron.*, vol. 29, no. 5, pp. 2380-2392, May 2014.

[50]   L. Zhang, P. Liu, A. Q. Huang, S. Guo and R. Yu, "An improved SiC MOSFET-gate driver integrated power module with ultra low stray inductances," in *proc. IEEE 5th Workshop on Wide Bandgap Power Devices and Applications (WiPDA)*, Albuquerque, NM, USA, 2017, pp. 342-345.

[51]   N. R. Mehrabadi, I. Cvetkovic, J. Wang, R. Burgos and D. Boroyevich, "Busbar design for SiC-based H-bridge PEBB using 1.7 kV, 400 a SiC MOSFETs operating at 100 kHz," in *proc. IEEE Energy Convers. Congr. and Expo. (ECCE)*, Milwaukee, WI, 2016, pp. 1-7.

[52]   S. Hazra, S. Madhusoodhanan, G. K. Moghaddam, K. Hatua and S. Bhattacharya, "Design Considerations and Performance Evaluation of 1200-V 100-A SiC MOSFET-Based Two-Level Voltage Source Converter," *IEEE Trans. Ind. Appl.* vol. 52, no. 5, pp. 4257-4268, Sep.-Oct. 2016.

[53] A. H. Wijenayake *et alia*, "Design of a 250 kW, 1200 V SiC MOSFET-based three-phase inverter by considering a subsystem level design optimization approach," in *proc. IEEE Energy Convers. Congr. Expo. (ECCE)*, Cincinnati, OH, 2017, pp. 939-946.

[54] J. Colmenares, D. Peftitsis, G. Tolstoy, D. Sadik, H. P. Nee and J. Rabkowski, "High-efficiency three-phase inverter with SiC MOSFET power modules for motor-drive applications," in *proc. IEEE Energy Convers. Congr. Expo. (ECCE)*, Pittsburgh, PA, 2014, pp. 468-474.

[55] L. Abbatelli, C. Brusca, and G. Catalisano, "How to fine tune your SiC MOSFET gate driver to minimize losses" [online] Available: http://www.st.com/content/ccc/resource/technical/document/application_note/7d/ 2b/9d/f0/88/07/4b/6f/DM00170577.pdf/files/DM00170577.pdf/jcr:content/transl ations/en.DM00170577.pdf   on Jan. 8, 2018.

[56] A. Rujas, V. M. López, L. Mir and T. Nieva, "Gate driver for high power SiC modules: design considerations, development and experimental validation," *IET Power Electron.*, vol. 11, no. 6, pp. 977-983, 29 5 2018.

[57] N. Oswald, P. Anthony, N. McNeill and B. H. Stark, "An Experimental Investigation of the Tradeoff between Switching Losses and EMI Generation With Hard-Switched All-Si, Si-SiC, and All-SiC Device Combinations," *IEEE Trans. Power Electron.*, vol. 29, no. 5, pp. 2393-2407, May 2014.

[58] Y. Jiang, W. Wu, Y. He, H. S. H. Chung and F. Blaabjerg, "New Passive Filter Design Method for Overvoltage Suppression and Bearing Currents Mitigation in a Long Cable Based PWM Inverter-Fed Motor Drive System," *IEEE Trans. Power Electron.*, vol. 32, no. 10, pp. 7882-7893, Oct. 2017.

[59] B. Bilgin et al., "Making the Case for Electrified Transportation," *IEEE Trans. Transportation Electrific.*, vol. 1, no. 1, pp. 4-17, Jun. 2015.

[60] "Variable speed drives by WEG electric corp." available at http://ecatalog.weg.net/files/wegnet/WEG-cfw11-system-drive-50019076-brochure-english.pdf

[61] F. Momen, K. Rahman and Y. C. Son, "Electrical Propulsion System Design of Chevrolet Bolt Battery Electric Vehicle," *IEEE Trans. Ind. Appl.*, 2018.

[62] IEEE Standard Test Procedure for Evaluation of Systems of Insulating Materials for Random-Wound AC Electric Machinery, ANSI C50.32- 1976 and IEEE Std 117-1974 (Reaffirmed 1984) (Revision of IEEE Std 117-1956), 1974, pp. i-22.

[63]   V. T. Buyukdegirmenci and P. T. Krein, "Induction Machine Characterization for Short-Term or Momentary Stall Torque," *IEEE Trans. Ind. Appl.*, vol. 51, no. 3, pp. 2237-2245, May-Jun. 2015.

[64]   R. B. Meinke, D. R. Kirk, and H. Gutierrez, "Hypersonic electromagnetic launch by constant-flux synchronous motor," in *proc. IEEE Int. Symp. Ind. Electron.*, Jul. 2006, vol. 3, pp. 2541–2548.

[65]   C. M. Laffoon, "Internally cooled generator coils increase ratings by onehalf," *Trans. Amer. Inst. Elect. Eng.*, vol. 70, no. 11, pp. 1013–1015, Nov. 1951.

[66]   Yifan Zhao and T. A. Lipo, "Space vector PWM control of dual three-phase induction machine using vector space decomposition," *IEEE Trans. Ind. Appl.*, vol. 31, no. 5, pp. 1100-1109, Sep.-Oct. 1995.

[67]   H. S. Che et al. "Current Control Methods for an Asymmetrical Six-Phase Induction Motor Drive," *IEEE Trans. Power Electron.*, vol. 29, no. 1, pp. 407-417, Jan. 2014.

[68]   L. Harnefors, S. E. Saarakkala and M. Hinkkanen, "Speed Control of Electrical Drives Using Classical Control Methods," *IEEE Trans. Ind. Appl.*, vol. 49, no. 2, pp. 889-898, Mar.-Apr. 2013.

[69]   A. G. Yepes, A. Vidal, J. Malvar, O. López and J. Doval-Gandoy, "Tuning Method Aimed at Optimized Settling Time and Overshoot for Synchronous Proportional-Integral Current Control in Electric Machines," *IEEE Trans. Power Electron.*, vol. 29, no. 6, pp. 3041-3054, Jun. 2014.

[70]   M. Masrur, "Penalty for fuel economy-system level perspectives on the reliability of hybrid electric vehicles during normal and graceful degradation operation," *IEEE Syst. J.*, vol. 2, no. 4, pp. 476–483, Dec. 2008.

[71]   P. Garg, S. Essakiappan, H. S. Krishnamoorthy and P. N. Enjeti, "A Fault-Tolerant Three-Phase Adjustable Speed Drive Topology With Active Common-Mode Voltage Suppression," *IEEE Trans. Power Electron.*, vol. 30, no. 5, pp. 2828-2839, May 2015.

[72]   Y. Song and B. Wang, "Survey on reliability of power electronic systems," *IEEE Trans. Power Electron.*, vol. 28, no. 1, pp. 591–604, Jan. 2013.

[73]   K. Ma et al., "Thermal loading and lifetime estimation for power device considering mission profiles in wind power converter," *IEEE Trans. Power Electron.*, vol. 30, no. 2, pp. 590–602, 2015.

[74] D. Hirschmann et al., "Reliability prediction for inverters in hybrid electrical vehicles," *IEEE Trans. Power Electron*., vol. 22, no. 6, pp. 2511–2517, 2007.

[75] H. Wang et al., "Toward reliable power electronics: Challenges, design tools, and opportunities," *IEEE Ind. Electron. Mag*., vol. 7, no. 2, pp. 17–26, 2013.

[76] Y. Song and B. Wang, "Evaluation Methodology and Control Strategies for Improving Reliability of HEV Power Electronic System," *IEEE Trans. Veh. Technol*., vol. 63, no. 8, pp. 3661-3676, Oct. 2014.

[77] United States nvironmental protection agency (EPA): vehicle and fuel emissions testing [Online]. Available: https://www.epa.gov/vehicle-and-fuel-emissions-testing/dynamometer-drive-schedules

[78] M. Ehsani, Y. Gao, and A. Emadi, Modern Electric, Hybrid Electric, and Fuel Cell Vehicles: Fundamentals, Theory, and Design, 2nd ed. Boca Raton, FL, USA: CRC Press, 2009, ser. Power Electronics and Applications Series.

[79] S. Y. Jung, J. Hong and K. Nam, "Current Minimizing Torque Control of the IPMSM Using Ferrari's Method," *IEEE Trans. Power Electron*., vol. 28, no. 12, pp. 5603-5617, Dec. 2013.

[80] W. N. W. A. Munim, M. J. Duran, H. S. Che, M. Bermúdez, I. González-Prieto and N. A. Rahim, "A Unified Analysis of the Fault Tolerance Capability in Six-Phase Induction Motor Drives," *IEEE Trans. Power Electron*., vol. 32, no. 10, pp. 7824-7836, Oct. 2017.

[81] Assessment of Thermal Control Technologies for Cooling Electric Vehicle Power Electronics [Online] Available: https://www.nrel.gov/transportation/assets/pdfs/42267.pdf

[82] M. H. Bierhoff and F. W. Fuchs, "Semiconductor losses in voltage source and current source IGBT converters based on analytical derivation," 2004 IEEE 35th Ann. Power Electron. Specialists Conf. (IEEE Cat. No.04CH37551), 2004, pp. 2836-2842 Vol.4

[83] H. Zhang, "Electro-Thermal Modelling of SiC Power electronics Systems", Ph.D. dissertation, electrical engineering Dept., The University of Tennessee, Knoxville, Dec. 2007.

[84] Thermal equivalent circuit models, [Online] Available: http://www.infineon.com/dgdl/InfineonAN2008_03_Thermal_equivalent_circuit _models-AN-v1.0

[85]   IEC TR 62380, Reliability Data Handbook-Universal Model for Reliability Prediction of Electronics Components, PCBs and Equipment, First Edition 2004. (Formerly RDF 2000 (UTE C 80-810))

[86]   P. F. Albrecht, J. C. Appiarius, R. M. McCoy, E. L. Owen and D. K. Sharma, "Assessment of the Reliability of Motors in Utility Applications - Updated," *IEEE Trans. Energy Convers.*, vol. EC-1, no. 1, pp. 39-46, Mar. 1986.

[87]   N. K. Ghai, "Design and application considerations for motors in steep-fronted surge environments," *IEEE Trans. Ind. Appl.*, vol. 33, no. 1, pp. 177-186, Jan/Feb 1997.

[88]   Y. Tang, "Analysis of steep-fronted voltage distribution and turn insulation failure in inverter-fed form-wound AC motor," *IEEE Trans. Ind. Appl.*, vol. 34, no. 5, pp. 1088-1096, Sep/Oct 1998.

[89]   P. Bidan, T. Lebey, G. Montseny and J. Saint-Michel, "Transient voltage distribution in inverter fed motor windings: experimental study and modeling," *IEEE Trans. Power Electron.*, vol. 16, no. 1, pp. 92-100, Jan 2001.

[90]   C. Petrarca, A. Maffucci, V. Tucci and M. Vitelli, "Analysis of the voltage distribution in a motor stator winding subjected to steep-fronted surge voltages by means of a multiconductor lossy transmission line model," *IEEE Trans. Energy Convers.*, vol. 19, no. 1, pp. 7-17, March 2004.

[91]   M. J. Scott et al., "Reflected wave phenomenon in motor drive systems using wide bandgap devices," in Proc. IEEE Workshop on Wide Bandgap Power Devices and Applications, Knoxville, TN, 2014, pp. 164-168.

[92]   O. Magdun, S. Blatt and A. Binder, "Calculation of stator winding parameters to predict the voltage distributions in inverter fed AC machines," in Proc. 9th IEEE Int. Symp. Diagnostics Elec. Mach., Power Electron. and Drives (SDEMPED), Valencia, 2013, pp. 447-453.

[93]   IEC/TS 61800-8 Ed. 1.0 en "Adjustable speed electrical power drive systems - Part 8: Specification of voltage on the power interface".

[94]   IEC 60034-18-41:2014 Rotating electrical machines - Part 18-41: Partial discharge free electrical insulation systems (Type I) used in rotating electrical machines fed from voltage converters - Qualification and quality control tests.

[95]   IEC 60034-18-42:2017 Rotating electrical machines - Part 18-42: Partial discharge resistant electrical insulation systems (Type II) used in rotating electrical machines fed from voltage converters - Qualification tests.

[96]   Yifan Tang, "Analysis of steep-fronted voltage distribution and turn insulation failure in inverter-fed form-wound AC motor*," IEEE Trans. Ind. Appl.*, vol. 34, no. 5, pp. 1088-1096, Sep./Oct. 1998.

[97]   H. Mirzaee, S. Bhattacharya, S. H. Ryu and A. Agarwal, "Design comparison of 6.5 kV Si-IGBT, 6.5kV SiC JBS diode, and 10 kV SiC MOSFETs in megawatt converters for shipboard power system," in *proc. Elect. Ship Technol. Symp.*, Alexandria, VA, Apr. 2011, pp. 248-253.

[98]   "Medium-Voltage Motors Ease Limits on Current Capacity and Power" [Online] Available: http://www.controleng.com/single-article/medium-voltage-motors-ease-limits-on-current-capacity-and power/8d0874a1d7bd0e7f6b2f7550ef3a33b4.html

[99]   A. Krings, G. Paulsson, F. Sahlén and B. Holmgren, "Experimental investigation of the voltage distribution in form wound windings of large AC machines due to fast transients," in Proc. XXII International Conference on Electrical Machines (ICEM), Lausanne, 2016, pp. 1700-1706.

[100]   L. Abbatelli, C. Brusca, and G. Catalisano, "How to fine tune your SiC MOSFET gate driver to minimize losses" [online] Available: http://www.st.com/content/ccc/resource/technical/document/application_note/7d/ 2b/9d/f0/88/07/4b/6f/DM00170577.pdf/files/DM00170577.pdf/jcr:content/transl ations/en.DM00170577.pdf   on Jan. 8, 2018.

[101]   A. Rujas, V. M. López, L. Mir and T. Nieva, "Gate driver for high power SiC modules: design considerations, development and experimental validation," *IET Power Electron.*, vol. 11, no. 6, pp. 977-983, 29 5 2018.

[102]   P. Anthony, N. McNeill and D. Holliday, "High-Speed Resonant Gate Driver With Controlled Peak Gate Voltage for Silicon Carbide MOSFETs," *IEEE Trans. Ind. Appl.*, vol. 50, no. 1, pp. 573-583, Jan.-Feb. 2014.

[103]   Z. Zhang, W. Zhang, F. Wang, L. M. Tolbert and B. J. Blalock, "Analysis of the switching speed limitation of wide band-gap devices in a phase-leg configuration," in *proc. IEEE Energy Convers. Congr. Expo. (ECCE)*, Raleigh, NC, 2012, pp. 3950-3955.

[104]   B. Zhang, S. Xie, J. Xu, Q. Qian, Z. Zhang and K. Xu, "A Magnetic Coupling Based Gate Driver for Crosstalk Suppression of SiC MOSFETs," *IEEE Trans. Ind. Electron.*, vol. 64, no. 11, pp. 9052-9063, Nov. 2017.

[105]   P. Nayak and K. Hatua, "Active Gate Driving Technique for a 1200 V SiC MOSFET to Minimize Detrimental Effects of Parasitic Inductance in the

Converter Layout," *IEEE Trans. Ind. Appl.*, vol. 54, no. 2, pp. 1622-1633, Mar.-Apr. 2018.

[106] P. Nayak and K. Hatua, "Parasitic Inductance and Capacitance-Assisted Active Gate Driving Technique to Minimize Switching Loss of SiC MOSFET*," IEEE Trans. Ind. Electron.*, vol. 64, no. 10, pp. 8288-8298, Oct. 2017.

[107] A. H. Wijenayake et al., "Design of a 250 kW, 1200 V SiC MOSFET-based three-phase inverter by considering a subsystem level design optimization approach," in *proc. IEEE Energy Convers. Congr. Expo. (ECCE)*, Cincinnati, OH, 2017, pp. 939-946.

[108] J. Wang, Y. Li and Y. Han, "Integrated Modular Motor Drive Design With GaN Power FETs," *IEEE Trans. Ind. Appl.*, vol. 51, no. 4, pp. 3198-3207, Jul.-Aug. 2015.

[109] X. Lu and F. Z. Peng, "Minimizing DC capacitor current ripple and DC capacitance requirement of the HEV converter/inverter systems," in *proc. IEEE Energy Convers. Congr. Expo.*, San Jose, CA, 2009, pp. 1191-1198.

[110] GaN Systems application note: "PCB Thermal Design Guide for GaN Enhancement Mode Power Transistors" [Online]. Available: https://gansystems.com/wp-content/uploads/2018/01/GN005_PCB-Thermal-Design-Guide-Enhancement-Mode-031815.pdf